Precambrian Research 430 (2025) 107943

Contents lists available at ScienceDirect

Precambrian Research

journal homepage: www.elsevier.com/locate/precamres

Metamorphic timescales of Neoproterozoic high-pressure granulites constrained by multi-mineral petrochronology: A case study from the Southern Brasília Orogen (SE Brazil)

Lorena de Toledo Queiroz [a,b,*], Brenda Chung Rocha [a], Bruno Vieira Ribeiro [b], Cauê Rodrigues Cioffi [a], Vinícius Tieppo Meira [c], Lucas Ramos Tesser [a], Armando Lucas Souza de Oliveira [a], Gyovana Patrícia Gonçalves Costa [a], George Luiz Luvizotto [d]

[a] Institute of Geosciences, University of São Paulo, São Paulo, Brazil
[b] Timescales of Mineral Systems Group, Curtin University, Perth, Australia
[c] Institute of Geosciences, University of Campinas, Campinas, Brazil
[d] Department of Geology, São Paulo State University, Rio Claro, Brazil

ARTICLE INFO

Keywords:
High-pressure granulite
Continental collision
Petrochronology
Andrelândia Nappe System
Carvalhos Klippe

ABSTRACT

Timescales of Neoproterozoic high-pressure granulites from the Carvalhos Klippe (Southern Brasília Orogen) were constrained through multi-mineral petrochronology. The high-grade metamorphism is related to continental collision processes during the assembly of West Gondwana and provides valuable insights on duration and rates of collisional settings in the Neoproterozoic. Most of the investigated samples comprises coarse-grained rutile-kyanite-garnet-orthoclase granulites, reaching peak metamorphic conditions of ~ 825 °C and 12 kbar, based on phase equilibrium modelling and Zr-in-rutile thermometry. Prograde to a near peak stage (630–620 Ma) was constrained by garnet Lu-Hf and U-Pb ages from high Y-HREE and low Th/U monazite domains. Low Y-HREE, high Th/U and Eu/Eu* monazite domains record the metamorphic peak (615–605 Ma) after substantial garnet growth, presence of melt and plagioclase consumption. The retrograde stage highlighted by high Y-HREE and Th/U and depleted Eu/Eu* monazite domains, reflects garnet dissolution and melt crystallization during the retrograde path (605–600 Ma). Zircon ages have a main cluster between 630 and 605 Ma, most likely related to near-peak cooling. Cooling ages obtained by rutile and apatite U-Pb and biotite Rb-Sr ranging from 570 to 540 Ma suggest slow cooling rates of 2–8 °C/Myr during the retrograde path, contrasting with the modern collisional orogens due to hotter mantle temperatures or low erosion rate and/or heat-producing elements concentration. This study demonstrates that the timescales of high-pressure granulites may provide a robust framework for understanding continental settings throughout the Earth's history.

1. Introduction

High-pressure granulites are geological witnesses of deep crustal metamorphic processes that occur during collisional orogenesis due to crustal subduction into mantle depths associated with crustal thickening (O'brien, 2008). High-pressure granulites started to appear rarely in the rock record at the Archean–Proterozoic boundary (e.g., Anderson et al., 2012, Li et al., 2023), possibly recording the beginning of collisional settings (Cawood et al., 2013). These metamorphic conditions (high-pressure granulite facies) are attained, at present, in plate margin collisional settings, suggesting that these Neoarchean rocks preserve evidence of plate tectonics on Earth since, at least, these times (e.g., Chowdhury and Chakraborty, 2019). However, these rocks record slow cooling-exhumation rates that differ from rapid cooling rates observed in modern tectonics, indicating different styles of plate tectonics acting on early Earth (Chowdhury and Chakraborty, 2019; Chowdhury et al., 2021; Cawood et al., 2022).

Comparing orogenic rates (i.e., cooling and exhumation rates) throughout Earth's history is a valuable way to evaluate secular changes (e.g., Chowdhury et al., 2021). However, reliably constraining these rates remains challenging. Petrochronology offers a robust approach for estimating pressure–temperature-time (*P-T*-t) trajectories from various

* Corresponding author.
E-mail address: lorena.toledo@alumini.usp.br (L.T. Queiroz).

https://doi.org/10.1016/j.precamres.2025.107943
Received 4 July 2025; Received in revised form 29 September 2025; Accepted 5 October 2025
Available online 9 October 2025

geological records (Engi et al., 2017). This approach has been successfully applied to high-grade metamorphic rocks, highlighting its relevance for studying the timescales of high-pressure metamorphism and, consequently, the processes of burial and exhumation during continental collision throughout Earth's evolution (e.g., Möller et al., 2000; Lotout et al., 2023). Otherwise, diffusion chronometry studies (Kohn and Penniston-Dorland, 2017) in major metamorphic minerals (e.g., garnet) have been used as a complementary tool to access the duration of metamorphic reactions (e.g., Liu et al., 2025), and to obtain the timescales of high-grade metamorphism (e.g., Xu et al., 2025) which also could be a complementary tool to understand metamorphic secular changes.

Recent advances in petrochronological techniques allow the simultaneous measurement of isotopic ratios and chemical composition extracted from the same ablated material by laser ablation split stream inductively coupled plasma mass spectrometry (LASS-ICP-MS) (Kylander-Clark et al., 2013; Kylander-Clark, 2017). The LASS-ICP-MS is a valuable tool to access multiple episodes of growth or consumption of major phases (i.e. garnet, feldspar), relating specific *P-T* conditions during metamorphic evolution constrained by thermodynamic modelling with dates/ages and trace element zoning in accessory phases (Hermann and Rubatto, 2003; Finger and Krenn, 2007; Holder et al., 2015; Hacker et al., 2015; Wang et al., 2015, 2017; Rocha et al., 2017; Hacker et al., 2019). Additionally, the recent development of triple quadrupole mass spectrometers enhanced in situ geochronology in several major metamorphic minerals such as garnet and biotite, which are important records of metamorphic evolution (Hogmalm et al., 2017; Ribeiro et al., 2023, 2024; Simpson et al., 2021; Zack and Hogmalm, 2016). Such advances allow the combination of multiple petrochronometers including monazite, zircon, titanite, rutile, apatite, garnet and biotite, with distinct stages of the metamorphism to constrain pressure–temperature-time-deformation (*P-T*-t-d) paths and, consequently, rates of tectono-metamorphic processes (e.g., Mottram et al., 2015; Wawrzenitz et al., 2015; Cioffi et al., 2019; Lotout et al., 2020; Ribeiro et al., 2022; Wang et al., 2023a; Wang et al., 2024).

The Southern Brasília Orogen (southeastern Brazil) is a collisional orogen associated with the Neoproterozoic assembly of West Gondwana (Campos Neto and Caby, 1999, 2000) and serves as a natural laboratory for studying orogenic processes in the late Cryogenian to Ediacaran. It exposes high-pressure felsic granulites characterized by rutile-kyanite-garnet-orthoclase assemblages with subordinate garnet-clinopyroxene mafic granulites (Campos Neto and Caby, 1999; Garcia and Neto, 2003; Cioffi et al., 2012; Reno et al., 2012; Motta and Moraes, 2017; Coelho et al., 2017; Li et al., 2021; Fumes et al., 2022; Benetti et al., 2024b). The available metamorphic and cooling ages for these high-pressure granulites range from 640 to 530 Ma (e.g., Campos Neto et al., 2010; Reno et al., 2012; Motta and Moraes, 2017; Coelho et al., 2017; Li et al., 2021; Fumes et al., 2022; Benetti et al., 2024a), making it difficult to reconstruct their metamorphic evolution due to overlapping age uncertainties and the lack of well constrained *P-T*-t correlations and textural evidence for equilibrium mineral assemblages.

To investigate the timescales of deep crustal processes associated with high-pressure metamorphism during continental collision, we applied a multi-mineral petrochronology approach to high-pressure felsic granulites from the Carvalhos Klippe in the Andrelândia Nappe System (Southern Brasília Orogen). These high-pressure granulites offer a unique opportunity to constrain the timescales of Neoproterozoic collisional settings, essential for understanding changes in plate tectonics throughout Earth's evolution and for providing empirical data to validate numerical geodynamic models (e.g., Chowdhury et al., 2021).

2. Geological setting

2.1. The Southern Brasília Orogen

The Brasília Orogen is part of the Tocantins Province (Almeida et al., 2000) and represents a Neoproterozoic collisional orogen associated with the amalgamation of West Gondwana during the Brasiliano-Pan-African orogenic event (Brito Neves et al.,1999; Cordani et al., 2003). The Brasília Orogen is divided into two segments: Northern Brasília Orogen (Fuck et al., 2017) and Southern Brasília Orogen (Valeriano et al., 2008, Valeriano, 2017).

The southernmost portion of the Brasília Orogen (Fig. 1) is a result of an Ediacaran collision between an active margin, the Paranapanema paleocontinent, onto a passive margin, the São Francisco paleocontinent (Brito Neves et al., 1999, Campos Neto and Caby, 1999, 2000; Trouw et al., 2000, 2013). It is characterized by a pile of sub-horizontal thick-skinned nappes transported towards the ENE to the São Francisco paleocontinent (Campos Neto et al., 2004). Three main tectonic domains are recognized from WSW to ENE: (i) Socorro-Guaxupé Nappe, interpreted as a root remnant of the magmatic arc domain developed in the active margin of the Paranapanema paleocontinent containing HT and UHT rocks (Campos Neto and Caby, 2000; Mora et al., 2014; Motta et al., 2021; Rocha et al., 2017, 2018; Rossi-Vieira et al., 2023; Tedeschi et al., 2017; Trouw et al., 2013; Vinagre et al., 2014; Trouw et al., 2000); (ii) Andrelândia Nappe System, consisting in subducted metasedimentary rocks divided into three high-pressure allochthons terrains (Campos Neto et al., 2010, 2011; Campos Neto and Caby, 1999; Reno et al., 2009, 2012; Coelho et al., 2017; Tedeschi et al., 2017; Frugis et al., 2018; Kuster et al., 2020); and (iii) the passive continental margin domain, consisting of Archean and Paleoproterozoic basement rocks, interpreted as part of the reworked São Francisco paleocontinent during the Neoproterozoic orogeny (Cioffi et al., 2016a,b, 2019; Amaral et al., 2019; Oliveira et al., 2019). It also includes the São Vicente Complex (Westin et al., 2016a) and the Carrancas Nappe System (Campos Neto et al., 2004, 2011; Trouw et al., 2013, Westin et al., 2019, Carvalho et al., 2020; Marimon et al., 2021, 2022, 2023). These units are composed of metasedimentary rocks related to the São Franciscan passive margin which extends to the Lima Duarte Nappe within the Ribeira Belt (Rocha et al., 2024a,b).

The Andrelândia Nappe System (ANS) occurs underneath the Socorro-Guaxupé Nappe and comprises subducted metasedimentary forming an inverted metamorphic pile, with amphibolite facies rocks at the base and high-pressure granulites at the top (Campos Neto and Caby, 1999, Campos Neto et al., 2010, 2011; Motta and Moraes, 2017; Coelho et al., 2017, Benetti et al., 2024a, b). Possible coesite remnants is described in the high-pressure granulite domain, suggesting metamorphism under ultra-high-pressure conditions (Campos Neto et al., 2024a,b), although this report has been contested (Schönig, 2024). The ANS is organized into three allochthonous terrains from top to bottom: i) the Três Pontas-Varginha Nappe (Campos Neto and Caby, 1999, 2000) and the Pouso Alto Nappe (northern and southern sectors, respectively), and the associated klippen (Aiuruoca, Carvalhos, and Serra da Natureza). These nappes and klippen are essentially composed of high-pressure granulites, mainly felsic granulites (rutile-kyanite-garnet-orthoclase granulite) and subordinate mafic granulites (garnet-clinopyroxene granulite) (Campos Neto et al., 2010; Cioffi et al., 2012; Reno et al., 2009, 2012; Motta and Moraes, 2017; Coelho et al., 2017; Li et al., 2021; Benetti et al., 2024b); ii) the Liberdade Nappe is predominantly composed of rutile-kyanite-garnet mica schists/gneisses at upper amphibolite metamorphic conditions (Trouw et al., 2000; Motta and Moraes, 2017); and iii) the Andrelândia Nappe, correlated in the western portion to the Carmo da Cachoeira Nappe, predominantly composed of metagraywackes and metapelites with metamorphic peak at middle to upper amphibolite facies (Trouw et al., 1983; Motta and Moraes, 2017; Frugis et al., 2018; Benetti et al., 2024a).

2.2. The Carvalhos Klippe

The Carvalhos Klippe (Supplementary Data 2 – Fig. S1) overlies the Liberdade Nappe and comprises metasedimentary and minor metamafic rocks recording high-pressure granulite facies peak metamorphism with

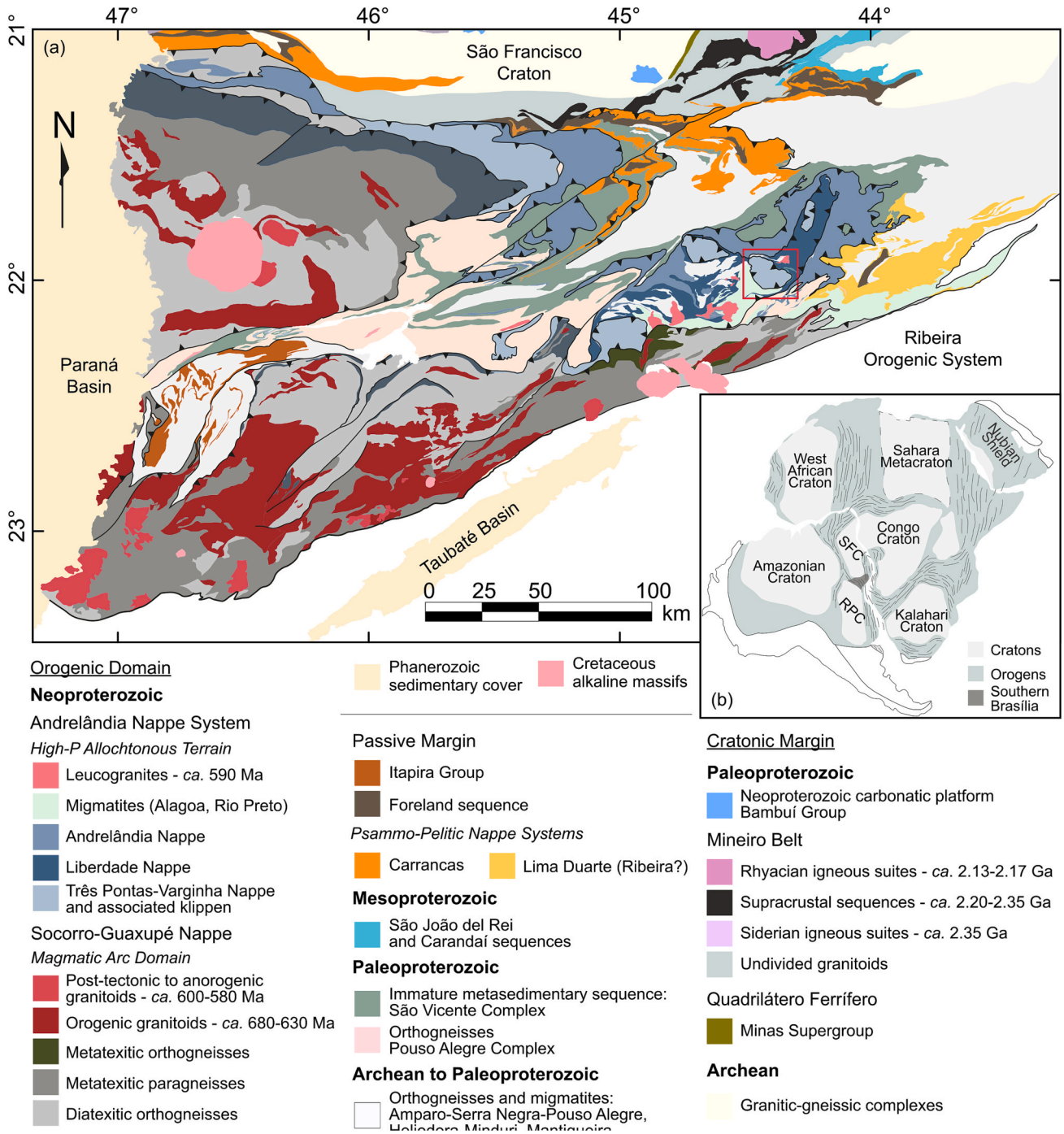

Fig. 1. (a) Geological map of the southernmost portion of the Brasília Orogen with the location of the Carvalhos Klippe in a red rectangle (modified from Campos Neto et al., 2011; Trouw et al., 2013; Cioffi et al., 2019); (b) West Gondwana contextualization (Gray et al., 2008).

evidence of partial melting at ~ 850 °C and 14 kbar (Campos Neto and Caby, 2000; Reno et al., 2009; Campos Neto et al., 2010; Cioffi et al., 2012). The predominant high-pressure felsic granulites preserve centimeter-scale metamorphic banding varying from fine/medium- to coarse-grained bands. These bands show a great variety of composition, reflecting in distinct colors (white to light, medium and dark gray) representing different proportions of rock-forming minerals, and diverse textures, including millimeter- to centimeter-scale garnet porphyroblasts. The Carvalhos Klippe can be divided into two main tectono-metamorphic units (Campos Neto et al., 2010): (1) the upper unit representing most of the exposed klippe; and (2) the lower unit predominantly exposed in the northwestern portion.

The upper unit is characterized by light-gray colored, coarse-grained rutile-kyanite-garnet-orthoclase granulite exhibiting garnet and kyanite porphyroblasts (Fig. 2 a,b,c) with heterogeneous banding (Fig. 2b). Additionally, fine-banded, white-colored rutile-garnet-orthoclase granulite with minor kyanite and higher plagioclase proportions occurs subordinately (Fig. 2d). The lower unit is composed predominantly of medium-gray-colored biotite-kyanite-garnet-orthoclase granulite with centimeter-sized garnet porphyroblasts (Fig. 2e). Subordinate dark-gray medium-grained plagioclase-garnet-biotite granulite also occurs (Fig. 2f).

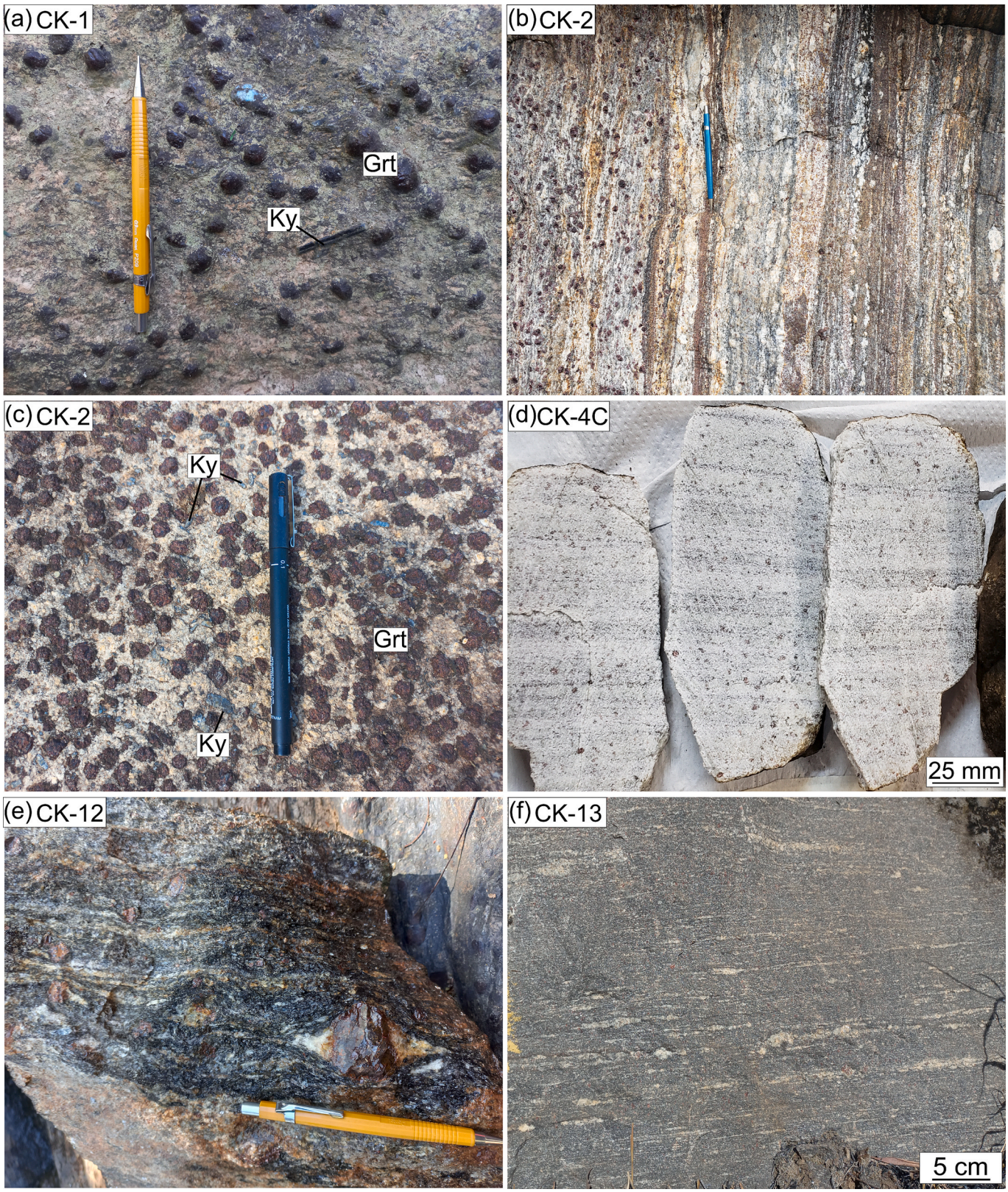

Fig. 2. Field aspects of the Carvalhos Klippe high-pressure felsic granulites. (a-c) light-gray rutile-kyanite-garnet-orthoclase granulite with garnet and kyanite porphyroblasts; (d) white-colored fine-banded rutile-garnet-orthoclase granulite; (e) medium-gray coarse-grained biotite-kyanite-garnet-orthoclase granulite with centimeter garnet porphyroblast; (f) dark-gray plagioclase-garnet-biotite granulite. Mineral abbreviations follow Whitney and Evans (2010).

3. Results

Seven samples of the representative lithotypes of high-pressure felsic granulites from the Carvalhos Klippe were selected for detailed petrochronological studies (Supplementary Data 2 – Table S1). All analytical data are provided in Supplementary Data 1 – Tables T1-T9 with methodological details in Supplementary Data 2 – Material A1-A8.

3.1. Petrography

A brief description of the selected samples for petrochronology is provided below. For additional petrography information on granulites from the Carvalhos Klippe see Campos Neto et al. (2010) and Cioffi et al. (2012).

Sample CK-1E is a coarse-grained porphyroblastic rutile-kyanite-garnet-orthoclase granulite, with garnet (up to 5 mm in diameter) and kyanite (up to 4 mm in length) porphyroblasts within a matrix composed of quartz (25–30 vol%), orthoclase (20–25 vol%) and rutile (5–8 vol%). Garnet (5–10 vol%) porphyroblasts encompass abundant prismatic rutile inclusions and display trails of acicular rutile defining internal foliation that truncate the external main foliation (Fig. 3a). Apatite, quartz, kyanite and ilmenite inclusions in garnet are present to a lesser extent (Fig. 4b). Garnet grains display resorbed rims, partially replaced by biotite + plagioclase + quartz ± kyanite (Figs. 3a, b). Kyanite (15–20 vol%) is mostly found as oriented porphyroblasts within the matrix, often with rutile and ameboid quartz and minor monazite inclusions. Common accessory minerals (< 5 vol%) include ilmenite, apatite, monazite and zircon.

Sample CK-2A is a medium-grained rutile-kyanite-garnet-orthoclase granulite with garnet (up to 3 mm in diameter) and kyanite (up to 1 mm in length) porphyroblasts and a matrix composed of quartz (20–25 vol %), orthoclase (15–20 vol%), rutile (5–8 vol%) and plagioclase (5–10 vol%). Garnet porphyroblasts display quartz, rutile, biotite, zircon, monazite, and apatite inclusions. Garnet also occurs as fine-grained crystals (up to 500 μm in diameter) in the granoblastic matrix (Fig. 3c). Kyanite (8–12 vol%) mostly occurs as inclusion-free porphyroblasts and fewer grains contain minor rutile, biotite, and quartz inclusions. Disequilibrium textures with biotite are observed at kyanite rims. Most of the biotite grains (5–8 vol%) occur replacing garnet and kyanite rims, interpreted as a retrograde phase. Common accessory minerals are ilmenite, monazite, zircon and apatite.

Sample CK-2B is a coarse-grained rutile-kyanite-garnet-orthoclase granulite displaying porphyroblastic texture, characterized by garnet (up to 9 mm in diameter) and kyanite (up to 4 mm in length) porphyroblasts within a matrix composed of quartz (15–25 vol%), orthoclase (20–25 vol%) and rutile (8–10 vol%). Garnet (20–25 vol%) porphyroblasts have prismatic and acicular rutile and ameboid quartz inclusions (Fig. 3d). Kyanite (10–15 vol%) porphyroblasts are oriented along the main foliation and have rutile and ameboid quartz inclusions. Locally, kyanite aggregates are present in the garnet rim. Late biotite (~5 vol%) is less abundant than in other samples and appears as tiny grains within matrix quartz and feldspar. Common accessory minerals include ilmenite, apatite, monazite and zircon.

Sample CK-2H is a medium to coarse-grained (kyanite)-rutile-garnet-orthoclase granulite exhibiting porphyroblastic texture (garnet porphyroblasts up to 3 mm in diameter) and matrix displaying nemato-granoblastic texture with quartz (25–35 vol%), orthoclase (20–25 vol %), plagioclase (20–25 vol%), rutile (5–10 vol%) and minor kyanite (< 5 vol%). Garnet (10–15 vol%) porphyroblasts are poikiloblastic with large inclusions of ameboid quartz, feldspar, biotite, and rutile (Fig. 3e). Biotite (< 5 vol%) is often observed around garnet rims and is also present as submillimeter thick layers defining the metamorphic foliation. Common accessory minerals include ilmenite, monazite, apatite, zircon and muscovite.

Sample CK-4C is a fine- to medium-grained, light gray to white-colored rutile-garnet-orthoclase granulite. Fine-grained garnet grains (up to 1 mm in diameter) (5–7 vol%) are usually free of inclusions, with only a few rounded quartz (Fig. 3f) and biotite inclusions. Matrix is mostly composed of quartz (30–35 vol%), perthitic orthoclase (20–25 vol%), plagioclase (10–15 vol%) and accessory kyanite, biotite and rutile. Biotite is only associated with small and randomly oriented crystals in the matrix or associated with the garnet rim. Other common accessory minerals are apatite, monazite, muscovite, opaques and zircon.

Sample CK-12B is a coarse-grained, porphyroblastic biotite-kyanite-garnet-orthoclase granulite characterized by large centimeter garnet porphyroblasts (up to 2 cm in diameter) and millimeter-scale kyanite crystals. Matrix is mostly composed of quartz (15–20 vol%), and orthoclase (10–15 vol%). Garnet porphyroblasts (30–35 vol%) are poikiloblastic with large inclusions of ameboid quartz, rutile, biotite, monazite, and ilmenite. Partial replacement of biotite + muscovite + kyanite along the garnet rims are common (Fig. 3g). Porphyroblastic kyanite is oriented in metamorphic foliation or in association with biotite and muscovite around the garnet rims (Fig. 3g). Biotite (5–8 vol %) is frequently associated with muscovite and kyanite at the garnet rims or as submillimeter lepidoblastic (biotite + muscovite) layers in the vicinity of kyanite porphyroblasts. Common accessory minerals are rutile, ilmenite, muscovite, monazite and zircon.

Sample CK-13 is a dark-gray fine- to medium-grained plagioclase-garnet-biotite granulite with kyanite, displaying medium- to coarse-grained garnet porphyroblasts (up to 2 mm in diameter) (15——20 vol %). Matrix is composed of orthoclase (25——30 vol%), biotite (~20 vol %), quartz (~20 vol%), plagioclase (10–15 vol%), and kyanite (5 vol%). Garnet porphyroblasts have kyanite, plagioclase, quartz, apatite, rutile, ilmenite, zircon, and pyrite inclusions. Garnet rims are partially replaced by biotite (Fig. 3h). Common accessory minerals include rutile, zircon, monazite, and xenotime.

3.2. Mineral chemistry and phase equilibrium modelling

The plagioclase-garnet-biotite granulite with kyanite (sample CK-13) is the granulite facies equivalent of the garnet-biotite-plagioclase-quartz schist of the Santo Antônio Schist unit (Trouw et al., 1983), identified in the lower grade, subsolidus amphibolite facies nappes from Andrelândia Nappe System. Due to the comparison of similar geochemical compositions between these rocks, Cioffi et al. (2012) suggested minimal degrees of melt extraction at high-grade (granulite facies) conditions. Consequently, sample CK-13 was likely less affected by melt loss and is the best candidate to represent the photolith composition, making it suitable for precise *P-T* estimation of the Carvalhos Klippe.

Garnet porphyroblast from sample CK-13 have compositional zoning, with core exhibiting higher contents of almandine (X*Alm* = 0.60 – 0.65), grossular (X*Grs* = 0.17) and spessartine (X*Sps* = 0.015 – 0.028) and lower contents of pyrope (X*Prp* = 0.15 – 0.21). Garnet mantle is depleted in grossular (X*Grs* = 0.08 – 0.14), in almandine (X*Alm* = 0.58 – 0.60) and spessartine (X*Sps* = 0.005 – 0.015) and enriched in pyrope (X*Prp* = 0.20 – 0.34). The garnet rim is characterized by higher contents of almandine (X*Alm* = 0.65 – 0.70) and spessartine (X*Sps* = 0.020 – 0.028) and lower contents of grossular (X*Grs* = 0.08 – 0.10) and pyrope (X*Prp* = 0.18 – 0.20) (Fig. 4). Matrix biotite grains have X*Mg* varying from 0.58 to 0.62 and Ti content ranging from 0.15 to 0.20 (*pfu*; per formula unit). Plagioclase grains are mostly oligoclase, with higher anorthite contents at the cores (X*An* = 0.20 – 0.30).

The modelled sample (CK-13) has a peak metamorphic assemblage of garnet + biotite + orthoclase + plagioclase + quartz + rutile + melt related to ~ 8 % of Fe as Fe_2O_3 and ~ 1.15 mol% of H_2O (Figs. 5a, b). That mineral assemblage is stable in a range of ≃11.0 – 14.5 kbar and ~ 820–835 °C (Fig. 5c). Peak conditions are compatible with garnet mantle isopleths of X*Grs* = 0.08 (Fig. 4b) and X*Prp* = 0.34 (Fig. 4d) and plagioclase composition of X*An* = 0.20 and reveal a *P-T* condition of ~ 12.4 kbar and ~ 825 °C (red star, Fig. 5d). The modelling reasonably simulates the modal proportion of ~ 23 vol% of garnet, ~25 vol% of

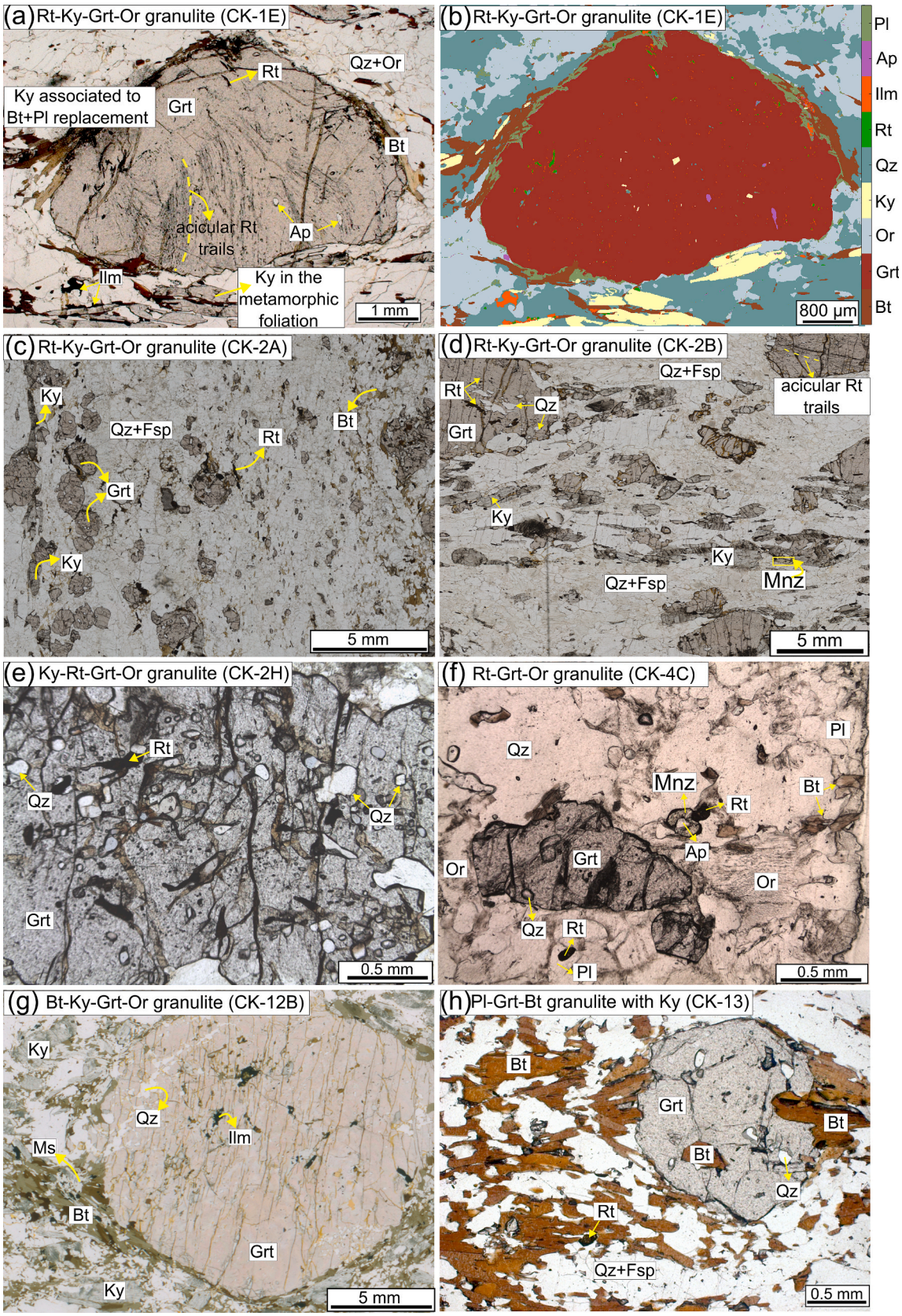

Fig. 3. Transmitted light, plane polarized photomicrographs of the studied high-pressure felsic granulites from the Carvalhos Klippe and (b) mineral phase map. (a,b) garnet porphyroblast with biotite replacement (CK-1E); (c) rutile-kyanite-garnet-orthoclase granulite (CK-2A); (d) rutile-kyanite-garnet-orthoclase granulite (CK-2b); (e) ameboid quartz and rutile inclusions in garnet porphyroblast (CK-2H); (f) rutile-garnet-orthoclase granulite (CK-4C); (g) biotite-kyanite-garnet-orthoclase granulite with garnet partial replacement of biotite + muscovite + kyanite (CK-12B); (h) plagioclase-garnet-biotite granulite with kyanite (CK-13). Mineral abbreviations follow Whitney and Evans (2010).

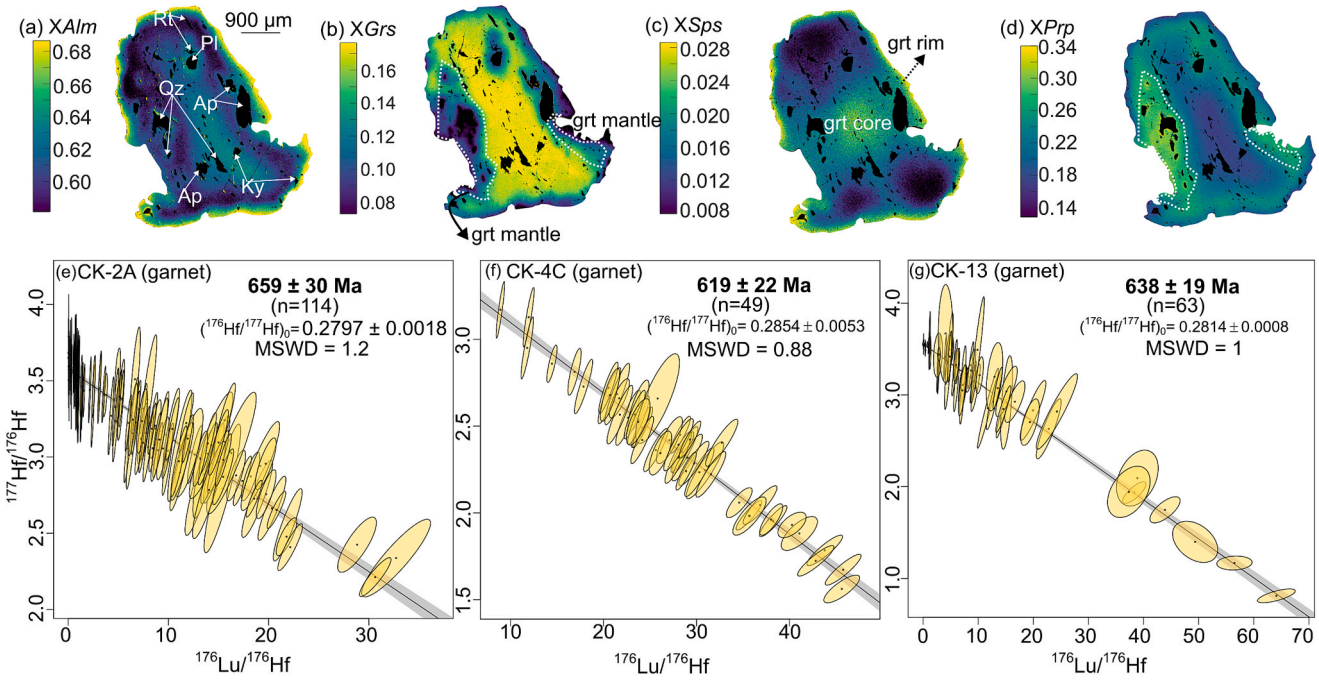

Fig. 4. Garnet compositional maps (sample CK-13). (a) almandine; (b) grossular; (c) spessartine; (d) pyrope. Mineral abbreviations follow Whitney and Evans (2010). Inverse Lu-Hf isochron plots of garnet from in situ measurements. (e) sample CK-2A; (f) sample CK-4C; (g) sample CK-13.

plagioclase, ~18 vol% of orthoclase and ~ 3 vol% of melt (Figs. 5e, f, g, h) as observed in the sample.

3.3. Garnet Lu-Hf geochronology

Two samples from the upper tectono-metamorphic unit (CK-2A, CK-4C) and one sample from lower unit (CK-13) were selected for in situ Lu-Hf garnet geochronology. The complete Lu-Hf dataset (n = 114 spots) from sample CK-2A yields an inverse Lu-Hf isochron date of 659 ± 30 Ma (MSWD = 1.2, n = 114) with an initial ^{176} Hf/ ^{177}Hf of 0.2797 ± 0.0018 (Fig. 4e).

Sample CK-4C displays small garnet crystals which yield an inverse Lu-Hf isochron age of 619 ± 22 Ma (MSWD = 0.88, n = 49) and ^{176} Hf/ ^{177}Hf initial ratio of 0.2854 ± 0.0053 (Fig. 4f). Garnet porphyroblasts of sample CK-13 yields and inverse Lu-Hf isochron date of 638 ± 19 Ma (MSWD = 1, n = 63) and initial ^{176} Hf/^{177}Hf of 0.2814 ± 0.0008 (Fig. 4g).

3.4. Monazite U-Pb and trace elements

In situ U-Pb and trace element monazite analyses of five samples from the upper tectono-metamorphic unit (CK-1E, CK-2A, CK-2B, CK-2H, CK-4C) and one sample from the lower unit (CK-12B) were conducted using LASS-ICP-MS. X-ray Ca, U, Th and Y compositional maps were used to guide the analyses on different compositional domains. U-Pb date errors are reported at 2 sigma level. Monazite ages are reported with decimal digits, as measurements were made using the multi-collector ICP-MS. Overdispersion dates are reported by the second uncertainty.

Trace element data were normalized to the chondrite following the McDonough and Sun (1995) values. Description of textural and zoning patterns, textural context, X-ray compositional maps and spot locations for all studied monazite grains and complementary chemical information are provided in Supplementary Data 2 – Table S2 and Supplementary Figs. S2-S13. Summarized chemical and isotopic results are provided in Supplementary Data 2 – Table S3.

3.4.1. Sample CK-1E

Six matrix monazite grains (M1, M2, M3, M4, M5 and M6) and one monazite inclusion in kyanite (M7) were investigated in sample CK-1E. Matrix monazite crystals (~100 to 300 µm in diameter) have irregular to subhedral shapes and are characterized by concentric zoning. Matrix cores are associated with the lowest Y-HREE concentrations (Y contents 72 – 1900 ppm, Gd_N/Lu_N = 39 – 1125, Gd_N/Lu_N mean = 516), Eu/Eu* ratios varying from 0.26 to 0.76 (Eu/Eu* mean = 0.63) and higher Th/U ratios from 4 to 64 (Th/U mean = 17) (Fig. 6a). Low Y-HREE matrix monazite cores yielded a lower intercept age of 605.8 ± 1.4 Ma (MSWD = 0.97, n = 27) (Fig. 6b).

Matrix monazite rims show enriched Y-HREE contents (Y contents from 294 to 2161 ppm, Y mean = 1241 ppm, Gd_N/Lu_N = 230 – 649; Gd_N/Lu_N mean = 439), Eu/Eu* varying from 0.17 to 0.76 (Eu/Eu* mean = 0.61) and low Th/U ratios ranging 9 – 37 (Fig. 6c). High Y-HREE matrix monazite rims display a lower intercept age of 600.3 ± 2.5 Ma (MSWD = 1.5, n = 18) (Fig. 6c).

One monazite inclusion in kyanite (M7) has ~ 160 µm in diameter and subhedral shape (Fig. 6d). It has homogeneous zoning evidenced for depleted Y-HREE contents (Y contents 477 – 1355 ppm, Y mean = 751 ppm, Gd_N/Lu_N ratios between 389 and 1171; Gd_N/Lu_N mean = 752), high Eu/Eu* with values between 0.59 and 0.69 and low Th/U from 7 to 16 (mean = 10) that encompass a U-Pb concordant data (102–106 % of concordance) yielding a weighted mean age of 609.8 ± 2.8 Ma (MSWD = 0.47; n = 4) (Fig. 6d).

3.4.2. Sample CK-2A

Three matrix monazite grains from sample CK-2A (M1, M7 and M8) (Fig. 7a) show lobate shape and concentric zoning encompassing Y-HREE enriched domain (Y contents of 1408 – 13842 ppm, Gd_N/Lu_N = 43 – 581), Eu/Eu* varying from 0.05 to 0.50 and Th/U ratios from 10 to 105 yield a weighted mean age of 606.8 ± 1.4 Ma (MSWD = 0.83, n = 20) (Fig. 7b).

Matrix monazite grains with Y-HREE depleted domain (Y contents of 425 – 1066 ppm, Gd_N/Lu_N = 970 – 1526), Eu/Eu* ranging from 0.27 to 0.33 and Th/U ratios from 58 to 86 display a weighted mean age of 613.3 ± 4.2 (MSWD = 0.99, n = 4). (Fig. 7c).

One monazite associated to retrograde biotite (M10, Fig. 7d) has an

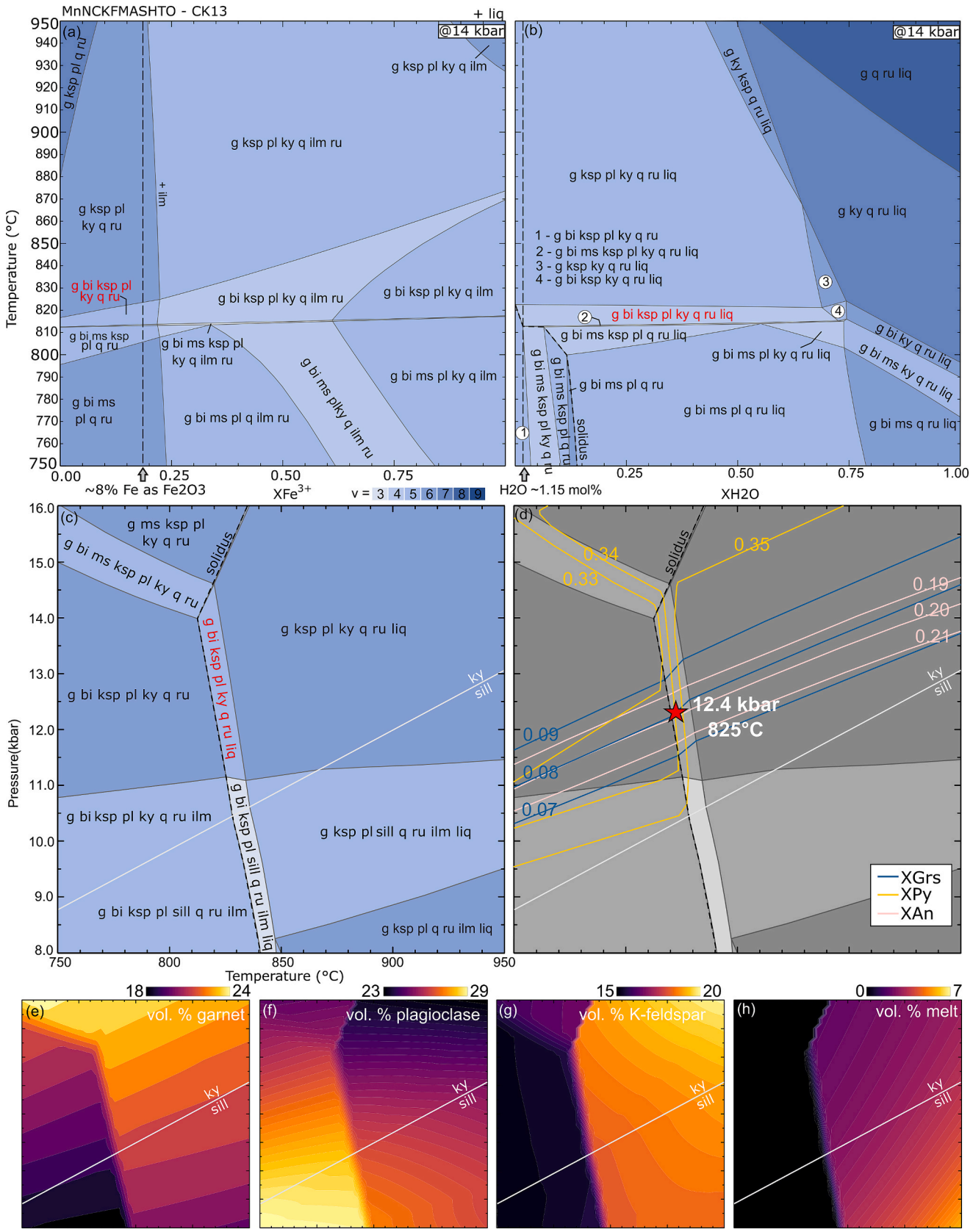

Fig. 5. Phase equilibrium modelling of sample CK-13. (a-b) T-X_{Fe3+} and T-X_{H2O} phase diagrams, respectively; (c) P-T phase diagram showing the stable field of the peak mineral assemblage; (d) P-T phase diagram with calculated grossular, pyrope and anorthite isopleths and red star is the peak P-T condition; (e-h) modelled modal mineral proportion (volume %) of garnet, plagioclase, K-feldspar and melt, respectively.

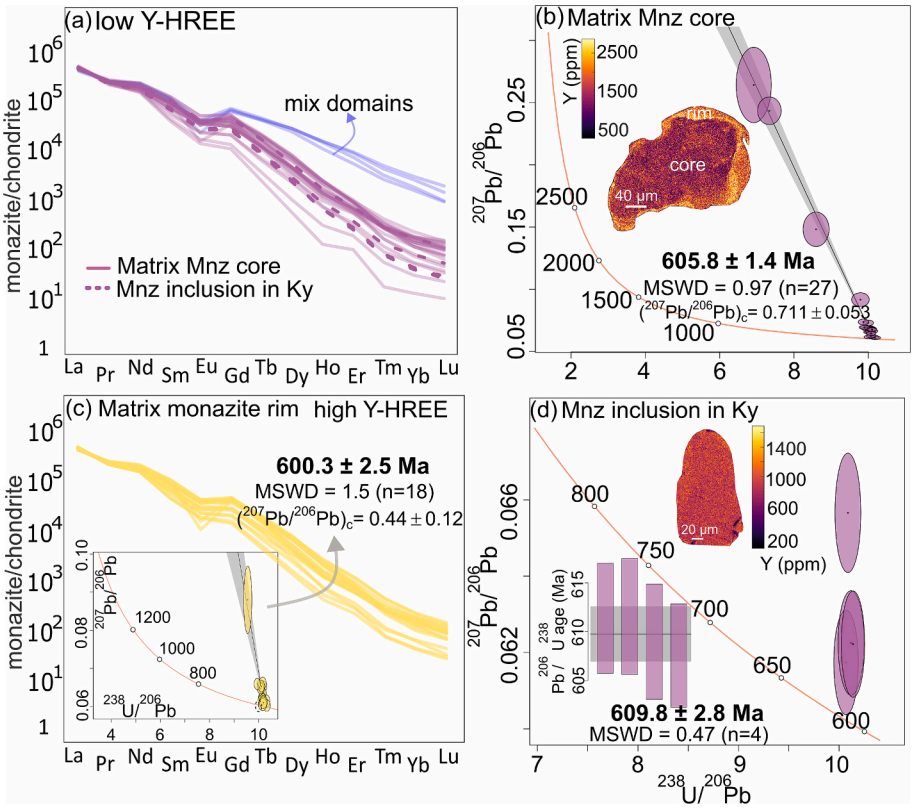

Fig. 6. REE and U-Pb monazite data for sample CK-1E. Chondrite-normalized REE plots for (a) low Y-HREE matrix monazite core and monazite inclusion in kyanite and (c) high Y-HREE matrix monazite rims within Tera-Wasserburg diagram in the lower left. Tera-Wasserburg diagram and representative quantitative compositional maps for (b) low Y-HREE matrix monazite cores, (d) low Y-HREE monazite inclusion in kyanite within Weighted mean age in the lower left.

irregular shape and concentric zoning, and it is characterized by Y-HREE depleted values (Y contents of 243 – 515 ppm, Gd_N/Lu_N = 1006 – 1355), Eu/Eu* ratios varying from 0.24 to 0.30 and Th/U values from 48 to 69. One data with high Y and HREE patterns is associated with the influence of the high Y rim domain that is near to the spot location. Monazite enclosed in retrograde biotite yields a weighted mean average age of 614.3 ± 2.7 (MSWD = 0.89, n = 8) (Fig. 7e).

Monazite grains included in garnet (M11 and M15) shows lobate shape and concentric to homogeneous zoning and shows depleted Y-HREE pattern (Fig. 7d), Y contents of 512 – 1575 ppm, Gd_N/Lu_N = 360 – 1674), Eu/Eu* values from 0.26 to 0.38 and Th/U ratio from 38 to 81 with a weighted mean age of 611.2 ± 2.5 (MSWD = 0.92, n = 11) (Fig. 7f).

3.4.3. Sample CK-2B

In sample CK-2B two matrix monazite grains (M8 and M13) were investigated (Fig. 8a). Monazite grain M8 have a diameter of up to 700 µm and shows subhedral shape with patchy zoning characterized by a Y-HREE-depleted domain (Y contents 168 – 3291 ppm, Gd_N/Lu_N = 188 – 1937), Eu/Eu* varying from 0.23 to 0.74 and Th/U ratios from 4 to 51 and a Y-HREE-enriched domain (Y contents ~ 14000 ppm, Gd_N/Lu_N = 42 – 58), Eu/Eu* varying from 0.37 to 0.47 and low Th/U ratios ranging from 10 to 14.

Matrix monazite M13 has a lobate shape with flat zoning defined by a Y-HREE-depleted domain (Y contents of 273 – 1630 ppm, Gd_N/Lu_N = 538 – 1590), Eu/Eu* ratios ranging from 0.23 to 0.39 and Th/U ratios ranging from 42 to 51.

One monazite enclosed in garnet mantle (M12) shows a lobate shape with patchy zoning (Fig. 8b) discriminated by low to intermediary Y and HREE concentrations (Y contents of 260 – 1600 ppm, Gd_N/Lu_N = 1066 – 1370) high Eu/Eu* (median = 0.73) and Th/U ratios varying from 4 to 8. By contrast, one high Y-HREE spot (Y = 15731 ppm, Gd_N/Lu_N = 89), with Eu/Eu* = 0.30 and low Th/U ratio of 5 was used to calculate a weighted mean age together with high-Y-HREE matrix monazite domain. The high Y-HREE and low Th/U domain were preserved in matrix monazite and monazite enclosed in garnet and yielded a weighted mean age of 621.0 ± 4.0 Ma (MSWD = 2.8, n = 3) (Fig. 8c).

The low Y-HREE domains on matrix monazite grains yield a lower intercept age of 611.6 ± 1.3 (MSWD = 1.8, n = 43) excluding an older concordant data (Fig. 8d). Additionally, the same lower intercept age of 612.3 ± 2.1 (MSWD = 0.41, n = 9) (Fig. 8e) with Stacey and Kramers (1975) Pb model anchored is registered on monazite inclusion in garnet with low Y-HREE and high Eu/Eu* domain.

3.4.4. Samples CK-2H, CK-4C and CK-12B

Two monazite crystals (M13 and M14) (~ 200 µm in diameter) in sample CK-2H were examined and display subhedral shapes. The matrix monazite (M13) exhibits concentric zoning, is associated with zircon and is surrounded by rutile. Monazite M13 yielded a lower intercept age of 609.1 ± 1.9 Ma (MSWD = 1.1; n = 12) with the exception of a younger outlier (589.57 ± 5.4 Ma) (Fig. 9a). The lower intercept age calculated is from a chemical domain with intermediated to high Y-HREE concentrations (Y contents of 201 – 14831 ppm; Y mean = 1993 ppm; Gd_N/Lu_N = 35 – 1272; Gd_N/Lu_N mean = 745), Eu/Eu* ratio mean of 0.27 and low Th/U (mean = 11). Monazite M14 with flat to concentric zoning is located at the garnet rim adjacent to zircon yielded a lower intercept age of 603.9 ± 1.8 Ma (MSWD = 1.7, n = 13) (Fig. 9b), calculated from a Y-HREE depleted domain (Y = 181 – 1124 ppm; Y mean = 297 ppm, Gd_N/Lu_N = 578 – 1898; Gd_N/Lu_N mean = 1483), with lower Eu/Eu* (mean = 0.15) and higher Th/U (mean = 31) ratios than the matrix monazite.

Five monazite crystals in the matrix (up to 300 µm in diameter) were analyzed in sample CK-4C (M2, M4, M8, M11 and M14). These crystals present shapes ranging from euhedral (e.g., M14) to lobate (e.g., M8)

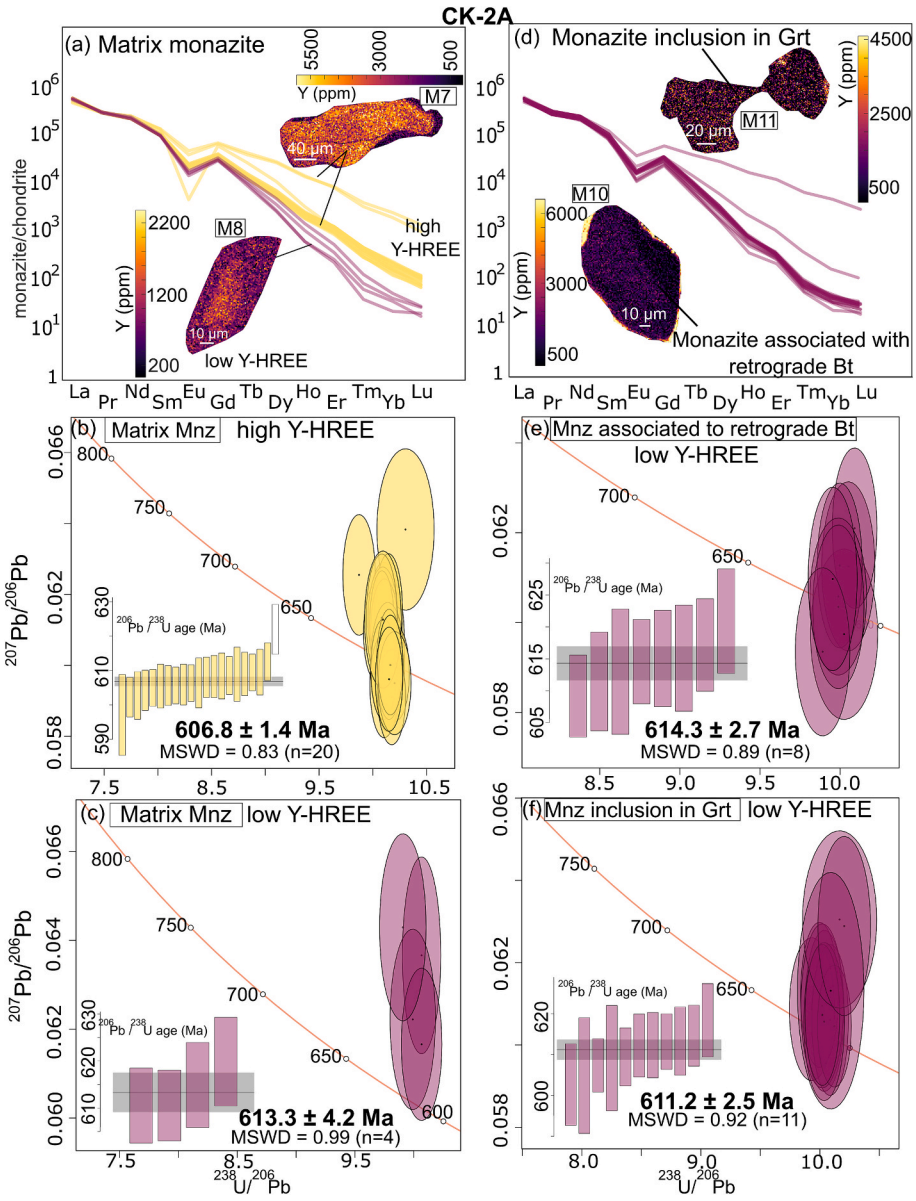

Fig. 7. REE and U-Pb monazite data for sample CK-2A. (a, d) Chondrite-normalized REE plots and representative quantitative compositional maps for matrix monazite and monazite inclusion in garnet, respectively. (b, c, e, f) Weighted mean age of (b) high Y-HREE matrix monazite, (c) low Y-HREE matrix monazite, (e) low Y-HREE monazite associated with retrograde biotite and (f) low Y-HREE monazite inclusion in garnet.

and display complex zoning patterns (e.g., M8 patchy zoning; Fig. 9c) and abundant apatite inclusions (M8, M11 and M14) and locally calcite (M2) and quartz-feldspar rounded inclusions (M8). Matrix grains which yield a lower intercept age of 606.8 ± 1.6 Ma (MSWD = 1.9; n = 50) (Fig. 9c) have Y contents ranging from 1323 to 11987 ppm (Y mean = 3619 ppm), Gd_N/Lu_N from 57 to 1048 (Gd_N/Lu_N mean = 532), low Eu/Eu* ratio with mean = 0.07 and high Th/U ratio (Th/U = 30 – 121; mean = 61). Patchy zoned monazite (M8) with large apatite inclusions (Fig. 9c) encompasses the oldest concordant data with a weighted mean age of 630.2 ± 2.5 Ma (MSWD = 0.33; n = 7) (Fig. 9d). This domain admits a high Y-HREE concentration ranging from 1877 to 11605 ppm (Y mean = 4664 ppm), Gd_N/Lu_N ratio from 86 to 908 (Gd_N/Lu_N mean = 532) of low Eu/Eu* mean = 0.11 (Eu/Eu* = 0.03 – 0.44) and high Th/U (mean = 43 and values between 35 and 61).

One matrix monazite adjacent to biotite and ilmenite (M6) and three monazite grains enclosed in garnet porphyroblast (M1, M2 and M9) were investigated in sample CK-12B. Mostly, the U-Pb results reveal a discordant dataset (Figs. 9e, f) compared to other analyzed samples. The matrix monazite M6 (~100 µm in diameter) has an irregular shape and provided a lower intercept age of 596.9 ± 4.8 Ma (MSWD = 2.7, n = 12) (Fig. 9e). This lower intercept age was calculated from all different chemical domains (Y = 513 – 14248 ppm; Gd_N/Lu_N = 45 – 1207), with Eu/Eu* higher than 0.40 and a low Th/U ratio (mean = 16). Monazite inclusions (up to 300 µm) in coarse-grained garnet porphyroblasts near to fractures have irregular shapes, are characterized by complex patchy zoning with different chemical domains (Y = 538 – 14402 ppm; Gd_N/Lu_N = 62 – 1601; Eu/Eu* > 0.36; Th/U mean = 18) which yielded a lower intercept age of 599.4 ± 1.5 Ma (MSWD = 1.3; n = 47) (Fig. 9f). Apparently, there is not any textural or chemical control on the distribution of ages, since all analyzed domains provided younger ages of *ca.* 600 Ma.

3.5. Zircon U-Pb and trace elements

Zircon grains from sample CK-13 display oscillatory zoned inherited cores and thick low luminescent rims with sector zoning (Fig. 10a). The

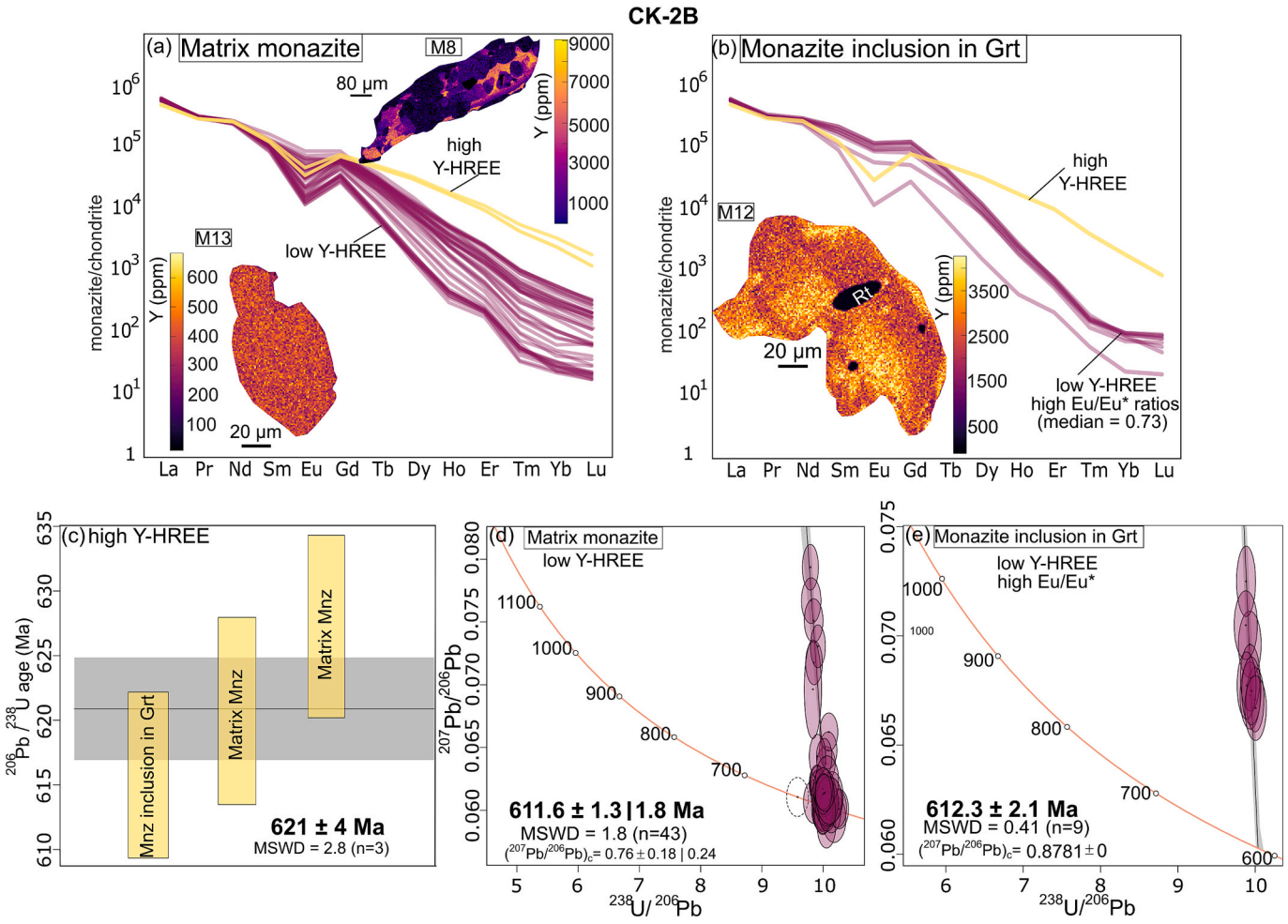

Fig. 8. REE and U-Pb monazite data for sample CK-2B. (a,b) Chondrite-normalized REE plots and quantitative compositional maps for matrix monazite and monazite inclusion in garnet, respectively; (c) Weighted mean average age of high Y-HREE monazite domain; (d-e) Tera-Wasserburg diagram for low Y-HREE matrix monazite and monazite inclusion in garnet, respectively.

cores show resorption textures characterized by irregular shapes and thin high luminescent recrystallization fronts at the core-rim boundaries. The inherited cores have high Th/U ratios (0.2–1.4) and steep chondrite-normalized HREE patterns with average Gd_N/Yb_N of 0.07, in contrast to sector zoned rims that display low Th/U ratios (0.01–0.03) and less steep HREE patterns with average Gd_N/Yb_N of 0.38 (Fig. 10b). Most of the inherited cores yield U-Pb dates ranging from 1000-700 Ma (Fig. 10c) with only two older concordant dates at *ca.* 2.4 and 2.1 Ga. Zircon rims yield U-Pb data that spread along concordia from *ca.* 640 to 595 Ma with a main cluster of $^{206}Pb/^{238}U$ dates within the 630–605 Ma range (Fig. 10c).

3.6. Rutile U-Pb geochronology and Zr-in-rutile thermometry

Trace element and U-Pb data were simultaneously acquired via LASS-ICP-MS from two samples from the upper unit (CK-1E and CK-2B) and two samples from the lower unit (CK-12B1 and CK-13). Rutile grains occur within the matrix and as inclusions in kyanite and/or garnet porphyroblasts.

Rutile grains from sample CK-1E yielded a concordia age of 550 ± 8 Ma (Fig. 11a) (MSWD = 1.9, n = 46). Uranium contents vary between 6 and 23 ppm, with smaller age uncertainties generally correlated to higher U values. Results from Zr-in-rutile thermometry (calibration of Tomkins et al., 2007 at 12 kbar) are within the 652–768 (±30) °C range, equivalent to Zr concentrations from 279 to 1007 ppm (Fig. 11a).

Rutile U-Pb analyses for sample CK-2B are slightly discordant. A lower intercept age of 556 ± 7 Ma (Fig. 11b) was calculated anchoring the uncorrected data through the initial $^{207}Pb/^{206}Pb$ value of the Stacey and Kramers (1975) model (MSWD = 3, n = 64) in the Tera-Wasserburg diagram. Uranium contents are within the 23–66 ppm range, with Zr concentrations varying from 400 to 1780 ppm and correspondent Zr-in-rutile temperatures ranging from 682 to 830 (±30) °C at 12 kbar (Fig. 11b).

Sample CK-12B rutile data yielded a concordia age of 551 ± 8 Ma (MSWD = 2, n = 35) (Fig. 11c). The U and Zr contents range from 10 to 26 ppm and from 383 to 1090 ppm, respectively. Estimated Zr-in-rutile temperatures are in the interval of 680 to 776 °C at 12 kbar (Fig. 11c).

Individual dates for sample CK-13 are moderately discordant, resulting in a lower intercept age of 571 ± 14 Ma (MSWD = 1, n = 13) (Fig. 11d). Most of the grains analyzed show relatively low U contents (5–10 ppm), while overall maximum values do not surpass 31 ppm. Zirconium contents of 258 to 1021 ppm result in Zr-in-rutile temperatures of 646 to 770 °C at 12 kbar (Fig. 11d).

3.7. Apatite U-Pb geochronology

Apatite U-Pb data were acquired for two samples from the upper unit (samples CK-2A and CK-2H). Tera-Wasserburg diagrams were plotted to calculate the lower intercept ages due to high common Pb to radiogenic Pb ratios in apatite. The dataset of both samples admits a good spread in $^{238}U/^{206}Pb$ ratios (Figs. 11e, f), which allows the calculations of a lower intercept age and an initial Pb composition in the upper intercept via

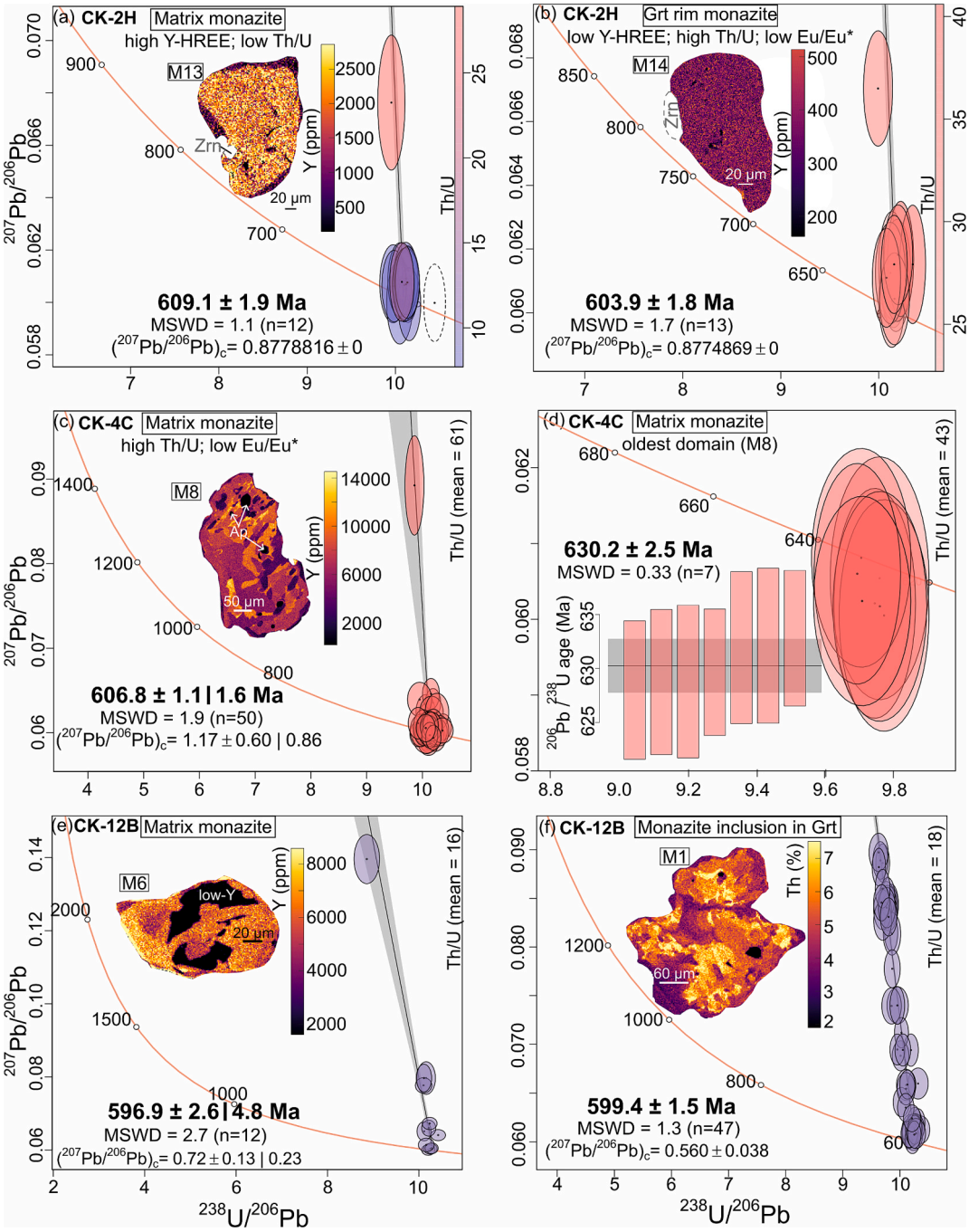

Fig. 9. U-Pb monazite data. (a,b) Tera-Wasserburg diagram and quantitative compositional maps of matrix monazite and garnet rim monazite, respectively (CK-2H); (c,d) Tera-Wasserburg diagram, representative quantitative compositional map and weighted mean diagram for matrix monazite (CK-4C); (e,f) Tera-Wasserburg diagram and representative quantitative compositional maps for matrix monazite and monazite inclusion in garnet, respectively (CK-12B). Color bar represents intensity of Th/U ratios.

linear regression (Ribeiro et al., 2020). Samples CK-2A and CK-2H yield lower intercept ages of 538 ± 12 Ma (MSWD = 1.5 and n = 33; Fig. 11e) and of 545 ± 12 Ma (MSDW = 1.4 and n = 32; Fig. 11f), respectively.

3.8. Biotite Rb-Sr geochronology

Biotite Rb-Sr geochronology was acquired for two samples from the upper unit (samples CK-2A and CK-2H). Sample CK-2A is characterized by an inverse isochron age of 537 ± 3 Ma (MSWD = 1.0, n = 49; Fig. 11g) with an anchored initial $^{87}Sr/^{86}Sr_i$ ratio of 0.73 ± 0.03 akin to common crustal rocks (Rösel and Zack, 2022). Sample CK-2H has biotite grains which yield a comparatively older inverse isochron date of 545 ± 3 Ma (MSWD = 0.6, n = 45; Fig. 11h) using the same anchoring approach. Anchoring the isochron to a typical crustal $^{87}Sr/^{86}Sr_i$ better constrains the isochrons for highly Rb-enriched minerals like the biotite grains from both samples (Rösel and Zack, 2022).

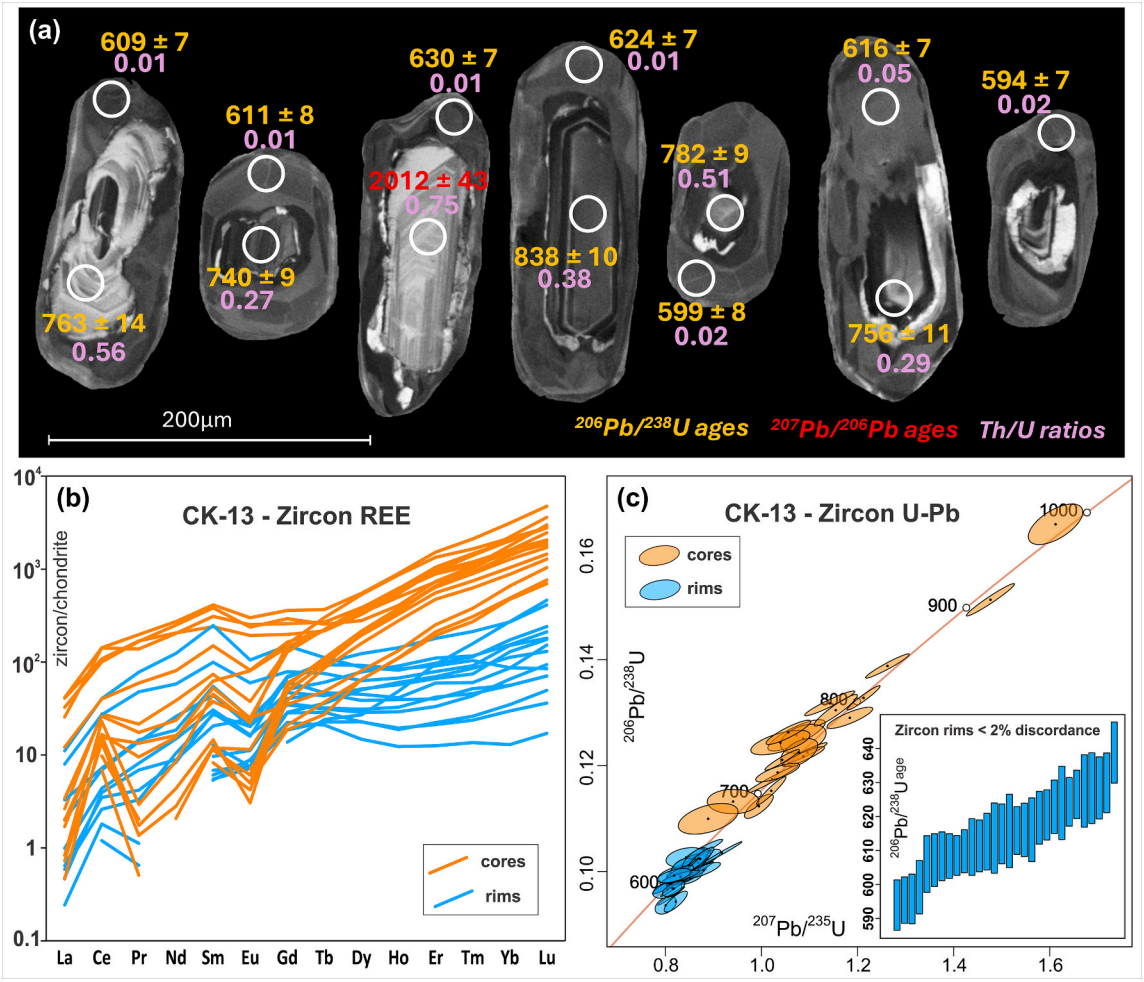

Fig. 10. (a) Cathodoluminescence images of representative zircon grains from sample CK-13; (b) Chondrite-normalized REE (McDonough and Sun, 1995) plot of zircon cores and rims analyses; (c) Wetherill U-Pb plot of zircon cores and rims analyses.

4. Discussion

4.1. Petrochronology of high-pressure granulites from the Carvalhos Klippe

The near-peak conditions for the Carvalhos Klippe of ~ 825 °C and 12 kbar were obtained from low grossular and high pyrope garnet mantle associated with the peak mineral assemblage of garnet + biotite + orthoclase + plagioclase + kyanite + quartz + rutile + melt (Figs. 4b and 7). The calculated Zr-in-rutile temperatures (Figs. 11a, d) are slightly lower and are interpreted as minimum temperatures.

Garnet is a key metamorphic mineral, and higher abundances are expected at peak metamorphic conditions (Fig. 5e). High spessartine cores may reflect growth in lower temperatures along the prograde path. The garnet Lu-Hf geochronology is a useful tool for tracing the timing of one of the most relevant metamorphic minerals (Tamblyn et al., 2022), especially in high-grade metamorphic rocks due to its high closure temperatures over 750 °C (e.g. Smit et al., 2013). Additionally, garnet is a sink for HREE and Y, hence linking garnet and monazite chemistry and age might shed light into the petrochronological relationship between these key chronometers in metamorphic rocks (e.g., Foster et al., 2000; Rubatto et al., 2006; Holder et al., 2015).

The garnet Lu-Hf isochron age of 638 ± 19 Ma (Fig. 4g) obtained from sample CK-13 most likely reflects the prograde to near-peak metamorphic conditions due to the prograde garnet growth preserved in high spessartine cores (Fig. 4c). Because Lu is strongly partitioned to garnet during early crystallization, the Lu-Hf age may reflect the prograde stages of garnet growth. In contrast, textural features such as ameboid quartz and plagioclase inclusions (Fig. 4a) may reflect near peak peritectic garnet growth. The fine-banded, white-colored rutile-garnet-orthoclase granulite (CK-4C) with inclusion-free small garnet crystals yields a garnet Lu-Hf isochron age of 619 ± 22 Ma (Fig. 4f), possibly recording the peritectic garnet growth during near-peak metamorphic conditions evidenced by rounded quartz inclusions which might be related to a melt phase (Fig. 3f). The rutile-kyanite-garnet-orthoclase granulite (CK-2A) produces an isochron age with high uncertainty of 659 ± 30 Ma due to lesser radiogenic isotopic ratios (Fig. 4e), which is also in agreement within uncertainty with the prograde stage age.

The growth of Y-HREE-enriched monazite is usually associated with prograde metamorphism before significant garnet growth or associated with garnet consumption during retrograde metamorphism (e.g. Cottle et al., 2009; Foster and Parrish, 2003; Hermann and Rubatto, 2003; Pyle and Spear, 2003; Spear and Pyle, 2002; Williams et al., 2007; Wang et al., 2015, 2017; Rocha et al., 2017). Monazite in the high-pressure felsic granulites of the Carvalhos Klippe records three distinct growth stages during the metamorphic evolution revealing a correlation to trace element content (especially Y and heavy rare earth element [HREE]) and Th/U ratios. Thorium contents in monazite chemical domains are also used to correlate growth in association to melt, once Th is mostly fractionated into monazite in the presence of melt (Dumond et al., 2015; Rocha et al., 2017), and it is expected to increase Th/U ratios in monazite associated with increasing metamorphic grade (Yakymchuk and Brown, 2019). We used those proxies to evaluate monazite

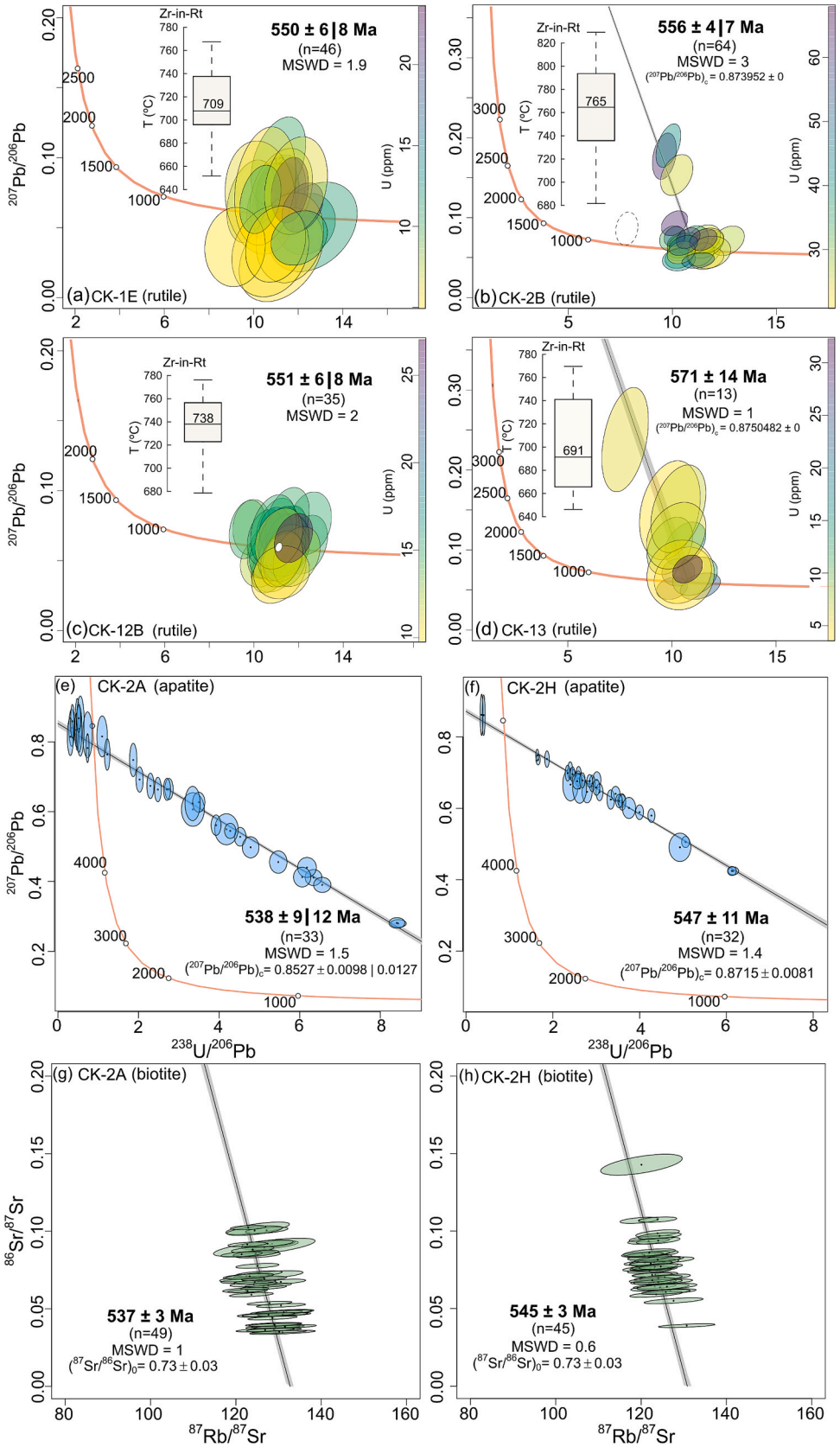

Fig. 11. U-Pb rutile Tera-Wasserburg diagrams and Zr-in-rutile thermometry. (a, c) concordia ages for samples CK-1E and CK-12B, respectively; (b,d) lower intercept ages with Stacey-Kramers common Pb correction for samples CK-2B and CK-13, respectively. Error ellipses are at the 2σ level. Color bar represents U contents in ppm. U-Pb apatite Tera-Wasserburg diagrams for samples (e) CK-2A and (f) CK-2H, respectively. Rb-Sr biotite inverse isochrons for samples (g) CK-2A and (h) CK-2H, respectively.

crystallization along the metamorphic path.

Stage I monazite is preserved in a few high Y-HREE and low Th/U domains in monazite inclusion in garnet porphyroblast and/or within the matrix, yielding U–Pb dates spanning from 630 to 620 Ma. We interpreted these ages (samples CK-2B, CK-4C) reflecting monazite growth before the biotite dehydration melting reaction responsible for abundant garnet growth and/or associated with xenotime breakdown during the prograde path (e.g., Shrestha et al., 2019). Additionally, the *ca.* 630 Ma age obtained in monazite with large apatite inclusions (grain M8; sample CK-4C) could represent monazite growth associated with apatite dissolution during prograde suprasolidus conditions (Johnson et al., 2015, Yakymchuk, 2017).

Stage II monazite is represented by low Y-HREE domains with high Th/U and Eu/Eu* ratios reflecting garnet growth, presence of melt and plagioclase consumption, respectively, during the high-pressure granulite facies metamorphism (Rubatto et al., 2006, 2013; Dumond et al., 2015; Holder et al., 2015; Hacker et al., 2015; Rocha et al., 2017) related to the biotite dehydration melting reaction (biotite + plagioclase + quartz = garnet + K-feldspar + melt) (Vielzeuf and Schmidt, 2001) at 615–605 Ma. These chemical domains are found in matrix monazite grains, as well as in monazite enclosed in kyanite and garnet porphyroblasts and monazite associated with retrograde biotite. Under (ultra) high-pressure metamorphic conditions, plagioclase is consumed (O'Brien and Rötzler, 2003) which affects the Eu concentration in accessory minerals (e.g., monazite) (Rubatto et al., 2006; Holder et al., 2015; Hacker et al., 2015). The trend of plagioclase consumption at the peak conditions is reinforced by thermodynamic modelling (Fig. 5f). Although, Eu concentrations in monazite can also be influenced by oxygen fugacity (fO_2) and/or fluid-rock interaction (Holder et al., 2020), we correlated the Eu/Eu* to plagioclase consumption by biotite dehydration during the high-pressure granulite metamorphic peak.

Stage III monazite (605–600 Ma) is characterized by high Y-HREE domains with high Th/U and low Eu/Eu* ratios, being interpreted to reflect garnet consumption during the retrograde path and melt crystallization during the cooling after high-grade metamorphism. A same age of *ca.* 600 Ma is also recorded in distinct chemical patterns in matrix monazite grains and exceptionally in monazite grains that are filling fractures in coarse-grained garnet porphyroblast (i.e., M1, M2, M14, sample CK-12B; Fig. 9f).These monazite patchy zoning domains likely reflect decoupling between ages and chemistry and may be affected by dissolution-reprecipitation driven by retrograde fluids that could have modified the U-Pb isotopic system (Seydoux-Guillaume et al., 2002; Harlov and Hetherington, 2010).

Zircon grains from sample CK-13 display thick sector zoned metamorphic overgrowths with low Th/U ratios and HREE-depleted patterns that yield a main cluster of dates ranging from 630 to 605 Ma (Fig. 10). The high age spread hampers a precise definition of metamorphic stages, but based on theoretical studies (Kelsey et al., 2008; Yakymchuk and Brown, 2014; Kohn et al., 2015) we interpret that the main zircon growth stage is related to cooling near-peak metamorphic conditions.

The cooling to temperatures below 600 ± 100 °C is constrained by U-Pb dating of rutile grains (Cherniak, 2000; Vry and Baker, 2006; Kooijman et al., 2010), which are part of the peak mineral assemblage. These ages overlap within uncertainty with U-Pb apatite ages (closure temperatures of ~ 450 ± 100 °C – Chamberlain and Bowring, 2001; Schoene and Bowring, 2007; Chew and Spikings, 2015; – see Oriolo et al. 2018 for additional information). The late stages of retrograde evolution are constrained by biotite Rb-Sr ages. In the analyzed samples (CK-2A, CK-2H), biotite is interpreted to be the result of biotite dehydration back-reactions at high-temperature. Therefore, Rb-Sr biotite ages are interpreted as cooling ages due to lower closure temperatures of the biotite Rb-Sr system (~350 ± 50 °C; Jäger, 1977; Verschure et al., 1980).

The obtained U-Pb rutile dates range between *ca.* 570 and 550 Ma which are slightly older than the U-Pb apatite and Rb-Sr biotite dates, ranging from *ca.* 550 to 540 Ma (Fig. 11). The 60–70 Myr interval between peak conditions of ~ 825 °C recorded by 615–605 Ma monazite ages and retrograde cooling to temperatures of ~ 350–450 °C recorded by U-Pb apatite and Rb-Sr biotite ages (Fig. 12), provides evidence for slow cooling rates of 5–8 °C/Myr in the high-pressure felsic granulites of the Carvalhos Klippe. The cooling rates would be even slower within the 2–8 °C/Myr range if only U-Pb rutile ages of 570–550 Ma are considered. Despite that apatite and rutile U-Pb ages can be reset (e.g., Ewing et al., 2013; Strachan et al., 2024) in polyphase metamorphic terranes (e.g., Wang and Guo, 2017; Wang et al., 2023a) there is not any evidence of a late thermal overprint in the present study. Therefore, it is assumed that the U-Pb rutile and apatite ages from the high-pressure granulites of the Carvalhos Klippe reflect cooling ages.

4.2. *Timescales of high-pressure granulite facies metamorphism along the Earth's secular evolution*

Paleoproterozoic high-pressure granulites of *ca.* 1.88 Ga associated with the Columbia formation in the North China Craton record *ca.* 90 Myr from the metamorphic peak at ~ 860–880 °C and 12 kbar to retrograde conditions of ~ 850 °C and 9 kbar (Li et al., 2023). Additionally, the age interval of 1.85–1.65 Ga obtained by zircon, titanite and rutile U-Pb ages of mafic dykes from the North China Craton that underwent high-pressure granulite metamorphism also record slow cooling rates of 1–3 °C/My (Wang et al., 2023a).

In contrast, Early Paleozoic high-pressure granulites related to Pangea formation record metamorphic peak of ~ 860–890 °C, 11–12 kbar at *ca.* 330 Ma and retrograde conditions of ~ 805–850 °C and 7 kbar at *ca.* 300 Ma yielding 30 Myr of exhumation recorded by zircon and monazite (Li et al., 2023). Using this local case study in China, it is possible to suggest a secular change in exhumation rates from the Paleoproterozoic to Paleozoic (Brown, 2014; Li et al., 2023).

Applying multi-mineral petrochronology to constrain the timescales of high-pressure granulites is a key approach to unraveling Earth's secular evolution offering relevant insights of tectonic changes (Brown and Johnson, 2018). Although diffusion chronology could be applied to constrain metamorphic timescales (e.g., Chakraborty, 2006; Xu et al., 2015), detailed multi-mineral petrochronological studies remain limited and can provide valuable information to improve our understanding of tectonic processes. In this study, we used multi-mineral petrochronology to shed light on the timing of metamorphism and cooling from natural records of continental collision during the Neoproterozoic.

The high-pressure felsic granulites from the Carvalhos Klippe record a metamorphic peak of ~ 825 °C and 12 kbar at 615–605 Ma constrained by U-Pb monazite ages, with apatite and rutile U–Pb and biotite Rb–Sr dates suggesting cooling rates of ≃2-8 °C/Myr (considering a simple linear and constant cooling path). Alternatively, the slight difference between rutile U-Pb and biotite Rb-Sr ages (570–550 Ma and 550–540 Ma, respectively) could suggest a final stage of fast cooling related to cooling rates of ~ 10–30 °C/My. High-pressure granulites associated to the Gondwana assembly during the Pan-African orogeny from the Mozambique Belt (Tanzania) report monazite and zircon peak ages of 655–610 Ma with slow cooling rates (2–5 °C/Myr) (Möller et al., 2000).

Peel-back orogenesis is a tectonic style which is associated with hotter mantle conditions operated during late Archean to early Proterozoic, which implies in shallow slab break-off that leads the mantle upwelling (Chowdhury et al., 2020, 2021). This mechanism operates under a hot and weak lithosphere which implies in long-lived metamorphism related to slow cooling (e.g., Chowdhury et al., 2021). The similar slow cooling rates (< 8 °C/Myr) related to the Gondwana amalgamation could be compatible and associated with thermo-mechanical models of peel-back driven orogenesis (Chowdhury et al., 2021).

The natural record of high-pressure granulites suggests that slow cooling of the lower collisional crust prevailed until the late Neoproterozoic. By contrast, monazite U-Pb ages of 26–19 Ma related to

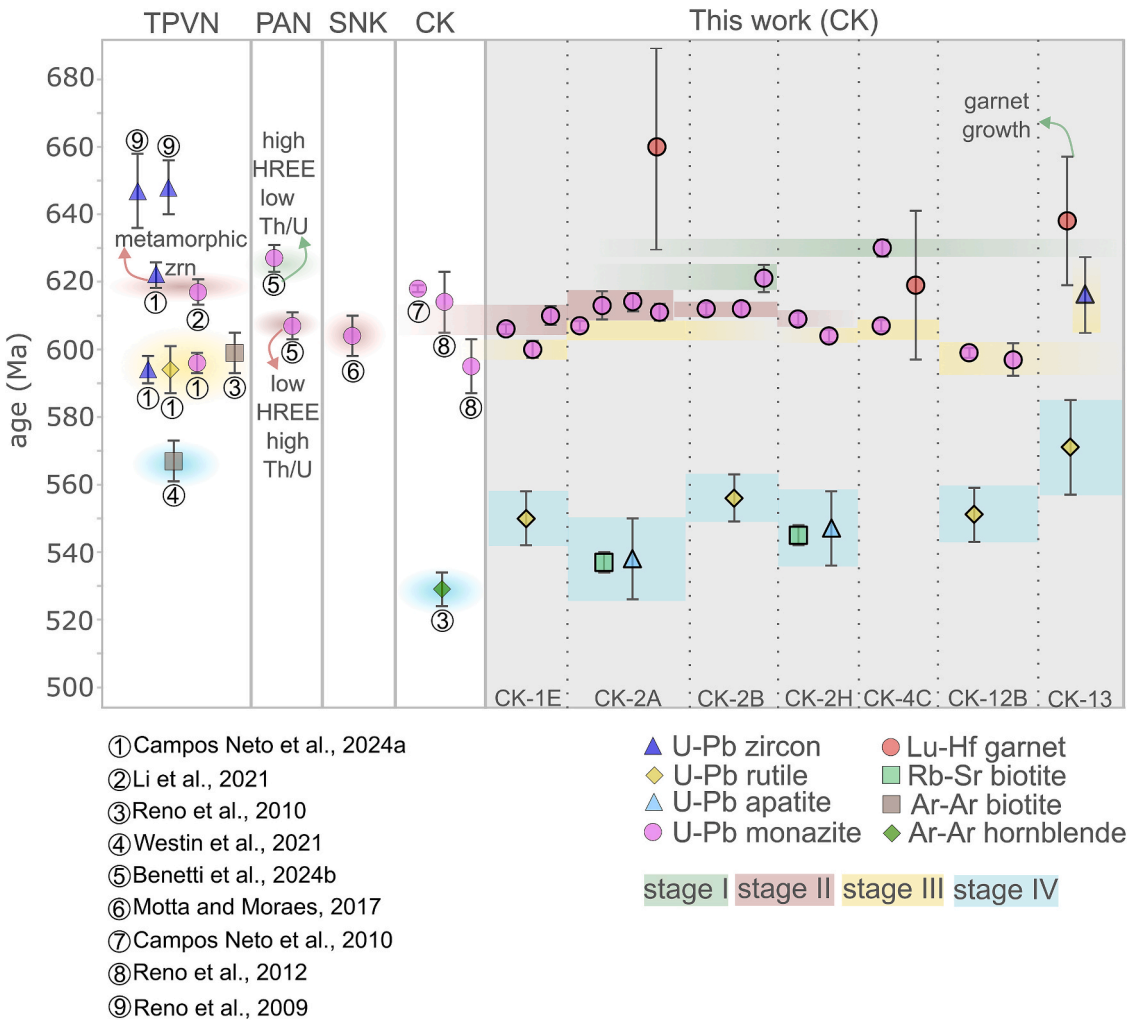

Fig. 12. Compilation of the geochronological data from high-pressure granulites of upper Nappes and associated klippen of the Andrelândia Nappe System: Três Pontas-Varginha Nappe (TPVN); Pouso Alto Nappe (PAN); Carvalhos Klippe (CK); Serra da Natureza Klippe (SNK).

granulite facies overprint associated to titanite and rutile U-Pb cooling ages of 12.5–9 Ma from the Ama Drime Massif (Central Himalaya) reflect fast cooling rates (*ca.* 20–30 °C/Myr) during the Cenozoic Himalayan continental collision (Wang et al., 2024). Similar cooling rates are also reported in the Greater Himalayan Crystalline Complex (Wang et al., 2015).

The high-pressure felsic granulites from the Namcha Barwa Complex, also associated with the India-Asian collision (i.e., Himalaya) display *ca.* 17 Myr of cooling history recorded through metamorphic peak at 25–24 Ma obtained by zircon U-Pb ages (Tian et al., 2019) and cooling to amphibolite facies at *ca.* 8 Ma constrained by hornblende $^{40}Ar/^{39}Ar$ ages (Ding et al., 2001) within cooling rates of ~ 20 °C/Ma contrasting with the Neoproterozoic record.

The cooling history from Paleoproterozoic to Cenozoic recorded by different high-pressure granulites may reflect the variations of mantle temperatures associated with the Earth's secular cooling or high contents of heat-producing elements (i.e., U, Th, K) which implies in a radiogenic heating and/or in different erosion rates (e.g., Clark et al., 2011). Modern orogenesis (e.g., Himalaya) display rapid cooling which differs from the Neoproterozoic example from our study, implying that collisional orogens in the Neoproterozoic remained hot longer than collisional orogens in the Cenozoic. This might be associated with mantle secular cooling or to climate consequences such as low erosion rates and compositional consequences as presence of heat-producing elements (Brown, 2014; Clark et al., 2011). The differences in cooling rates could be also related to thermal structures such as lithospheric extension which would result in long-lived cooling (Wang et al., 2023a and references therein). Additionally, contrasting cooling rates might be influenced by different mechanisms of exhumation resulting in fast or protracted cooling (Wang and Guo, 2017).

4.3. *Timing of continental collision in the southernmost portion of Brasília Orogen*

The compilation of the geochronological data from the high-pressure granulites from the Andrelândia Nappe System reveals the metamorphic evolution and cooling stages (Fig. 12). Our monazite dataset defines prograde metamorphic ages of 630–620 Ma, based on analyses of high Y-HREE, and low Th/U monazite domains interpreted as a growth stage associated with lower garnet proportions. The Lu-Hf garnet ages (Figs. 4e, g) probably reflect the prograde to near-peak conditions (stage I), which agree within uncertainty with the high Y-HREE, and low Th/U monazite domains at 630–620 Ma, interpreted to reflect a growth stage before biotite breakdown and peritectic garnet growth along with melt. Similarly, a prograde age of *ca.* 620 Ma has been described in high HREE and low Th/U monazite grains from the Pouso Alto Nappe (Benetti et al., 2024b).

Available zircon and monazite U-Pb ages from the upper nappes and associated klippen suggest contemporaneous high-pressure metamorphic peak of ~ 825–1000 °C and ~ 12–20 kbar (stage II) in the

Pouso Alto Nappe (Benetti et al., 2024b), Carvalhos (Campos Neto et al., 2010; Reno et al., 2012; this work) and Serra da Natureza klippen (Motta and Moraes, 2017), while the Três Pontas-Varginha Nappe records slightly older ages with ages of *ca.* 640–620 Ma interpreted to be associated to the peak conditions (Reno et al., 2009; Li et al., 2021; Campos Neto et al., 2024a). Ages obtained in low Y-HREE, high Th/U and Eu/Eu* domains from matrix monazite and monazite inclusions in garnet (this work) are interpreted to reflect crystallization at *ca.* 615–605 Ma under high-pressure granulite conditions.

The 600–590 Ma ages reported in the Três Pontas-Varginha Nappe, including monazite, zircon and rutile U-Pb ages (Campos Neto et al., 2024a) and ^{40}Ar-^{39}Ar biotite ages (Reno et al., 2010), are interpreted to reflect retrograde conditions. Similarly, *ca.* 605–600 Ma ages are reported in high Y-HREE, high Th/U and low Eu/Eu* monazite grains (this work; Reno et al., 2012) for the Carvalhos Klippe which are interpreted to reflect garnet resorption and melt crystallization (stage III). In this work, the cooling stage (stage IV) was addressed by using lower closure temperature geochronometers, including rutile and apatite U-Pb and biotite Rb-Sr, with ages ranging from 570 to 540 Ma. Those ages are equivalent to hornblende ^{40}Ar-^{39}Ar ages from the mafic high-pressure granulites from the Carvalhos Klippe (Reno et al., 2010) and biotite ^{40}Ar-^{39}Ar ages from the Três Pontas-Varginha Nappe (Westin et al., 2021) (Fig. 12). Additionally, high-pressure granulites (garnet + kyanite + rutile + K-feldspar + quartz ± plagioclase) from the Passos Nappe (Southern Brasília Orogen) record monazite ages related to metamorphic peak of *ca.* 635 Ma and rutile U-Pb ages of *ca.* 590 Ma, defining similar cooling rates of ~ 5 °C/Myr (Fumes et al., 2022).

5. Conclusions

Multi-mineral petrochronology of Neoproterozoic high-pressure felsic granulites from the Carvalhos Klippe in the Southern Brasília Orogen provide a timescale of 90 Myr from prograde to cooling history (630–540 Ma). Garnet Lu-Hf ages (660–620 Ma) represent the timing of prograde to near-peak conditions. Also, monazite chemical domains with a complex history of (re)crystallization and dissolution-precipitation evidence by Y, HREE, Th/U and Eu/Eu* patterns offer a correlation to prograde (620–630 Ma), peak (615–605 Ma) and retrograde (605–600 Ma) stages. Zircon ages spanning 630–605 Ma may be related to cooling near-peak metamorphic conditions. Rutile ages (570–550 Ma), apatite ages (550–540 Ma) and retrograde biotite ages (550–540 Ma) unravel 60–70 Myr of cooling history associated with slow cooling rate of 2–8 °C/Ma.

The high-pressure felsic granulites of the Carvalhos Klippe record a long-lived metamorphic evolution related to continental collisional in West Gondwana. These high-pressure granulites may reflect hotter mantle conditions in the Neoproterozoic or low erosion rates and increase concentration of heat-producing elements. We evaluated the impact of a robust petrochronological dataset to compare different high-pressure granulite timescales to comprehend behavior of collisional settings, and consequently, how plate tectonics dynamics change along the Earth's evolution. These multi-mineral petrochronological insights provide valuable empirical data that can be integrated into thermo-mechanical numerical models to enhance our understanding of continental collision and the framework of plate tectonics throughout Earth's evolution.

CRediT authorship contribution statement

Lorena de Toledo Queiroz: Writing – review & editing, Writing – original draft, Visualization, Investigation, Formal analysis. **Brenda Chung Rocha:** Writing – review & editing, Visualization, Validation, Supervision, Project administration, Investigation, Funding acquisition, Conceptualization. **Bruno Vieira Ribeiro:** Writing – review & editing, Validation, Resources, Methodology, Investigation, Formal analysis. **Cauê Rodrigues Cioffi:** Writing – review & editing, Visualization, Validation, Project administration, Investigation, Funding acquisition, Conceptualization. **Vinícius Tieppo Meira:** Writing – review & editing, Validation, Investigation, Funding acquisition. **Lucas Ramos Tesser:** Writing – review & editing, Visualization, Investigation, Formal analysis. **Armando Lucas Souza de Oliveira:** Writing – review & editing, Visualization, Investigation. **Gyovana Patrícia Gonçalves Costa:** Writing – review & editing, Investigation. **George Luiz Luvizotto:** Writing – review & editing, Resources, Methodology, Investigation.

Declaration of competing interest

The authors declare that they have no known competing financial interests or personal relationships that could have appeared to influence the work reported in this paper.

Acknowledgments

This study was funded by São Paulo Research Foundation (FAPESP) through grants 2021/09437-9 to B.C.R; 2023/06385-3 to C.R.C; 2021/00967-5 to V.T.M and FAPESP scholarships 2022/07116-3, 2022/14877-0, 2023/17836-6 to L.T.Q; 2021/06106-1 to L.R.T; 2023/17675-2 to A.L.S.O. and 2023/08262-6 to G.P.G.C. We sincerely thank Renée Tamblyn for all the help, Dr. Mahyra Tedeschi for the discussion which enriched this work and assistance with XMapTools,and we also thank the Timescales of Mineral System Group (Curtin University). The authors appreciate the reviews of Jia-Min Wang and the anonymous reviewer that contributed for the improvement of this work. We are grateful for the editorial remarks of Marly Babinski. Also, this work acknowledges Liz Zanchetta (LCT-Poli), Brad McDonald (Geohistory Facility LA-ICP-MS) and Dr. Kai Rankenburg (Geohistory Facility LA-ICP-MS).

Appendix A. Supplementary data

Supplementary data to this article can be found online at https://doi.org/10.1016/j.precamres.2025.107943.

Data availability

All data are provided in the supplementary material

References

Anderson, J.R., Payne, J.L., Kelsey, D.E., Hand, M., Collins, A.S., Santosh, M., 2012. High-pressure granulites at the dawn of the Proterozoic. Geology 40 (5), 431–434.
Almeida, F.F.M., Brito-Neves, B.B., Carneiro, C.D.R., 2000. The origin and Evolution of the South American Platform. Earth Sci. Rev. 50, 77–111.
Benetti, B., Neto, M.D.C.C., Carosi, R., Luvizotto, G., Iaccarino, S., Montomoli, C., 2024a. In-sequence tectonic evolution of Ediacaran nappes in the southeastern branch of the Brasília Orogen (SE Brazil). Constraints from metamorphic iterative thermodynamic modeling and monazite petrochronology. Lithos 464, 107459.
Benetti, B., Neto, M.D.C.C., Carosi, R., Iaccarino, S., Luvizotto, G.L., Montomoli, C., Langone, A., 2024b. Continental subduction and exhumation of the lower crust in a hot orogen. Insights from high-pressure (ultra) high-temperature granulite in the Pouso Alto Nappe, Southeast Brazil. Lithos 482, 107720.
Brito Neves, B.B., Campos Neto, M.C., Fuck, R.A., 1999. From Rodinia to Western Gondwana. an approach to the Brasiliano-Pan African Cycle and orogenic collage. Episodes 22, 155–166.
Brown, M., 2014. The contribution of metamorphic petrology to understanding lithosphere evolution and geodynamics. Geosci. Front. 5 (4), 553–569.
Brown, M., Johnson, T., 2018. Secular change in metamorphism and the onset of global plate tectonics. Am. Mineral. 103 (2), 181–196.
Campos Neto, M.C., Caby, R., 1999. Neoproterozoic high-pressure metamorphism and tectonic constraint from the nappe system south of the São Francisco Craton, southeast Brazil. Precambr. Res. 97, 3–26.
Campos Neto, M.C., Caby, R., 2000. Terrane accretion and upward extrusion of high-pressure granulites in the Neoproterozoic nappes of Southeast Brazil. Petrological and Structural Constraints. Tectonics 14, 669–687.
Campos Neto, M.C., Basei, M.A.S., Vlach, S.R.F., Caby, R., Szabó, G.A.J., Vasconcelos, P., 2004. Migração de orógenos e superposição de orogêneses. Um esboço da colagem Brasiliana no sul do Cráton do São Francisco, SE – Brasil. Revista Do Instituto De Geociências – USP, Geologia USP, Série Científica 4 (1), 13–40.

Campos Neto, M.C., Cioffi, C.R., Moraes, R., Motta, R.G., Siga Jr, O., Basei, M.A.S., 2010. Structural and metamorphic control on the exhumation of high-P granulites. the Carvalhos Klippe example, from the oriental Andrelândia Nappe System, southern portion of the Brasília Orogen. Brazil. Precambrian Research 180, 125–142.
Campos Neto, M.C., Basei, M.A.S., Janasi, V.A., Moraes, R., 2011. Orogen migration and tectonic setting of the Andrelândia Nappe system. an Ediacaran western Gondwana collage, south of São Francisco craton. J. S. Am. Earth Sci. 32 (4), 393–406.
Campos Neto, M. C., Frugis, G. L., Westin, A., Caby, R., Nobre, A. G., Brugier, O., & Ando, R. A. 2024a. Passive continental margin subducted to mantle depths. Coesite-bearing metasedimentary rocks from the Neoproterozoic Brasília Orogen, West Gondwana margin. Precambrian Research, 410, 107469.
Campos Neto, M., Frugis, G., Westin, A., Caby, R., Nobre, A., Bruguier, O., Ando, R., 2024b. Reply to "comment on. Passive continental margin subducted to mantle depths. Coesite-bearing metasedimentary rocks from the Neoproterozoic Brasília Orogen, West Gondwana margin" by Schönig 2024. Precambr. Res. 413, 107577.
Carvalho, B.R.B.M., Trouw, R.A.J., Vinagre, R., Ribeiro, A., Heilbron, M., Marimon, R.S., 2020. Microstructural and metamorphic Evolution of the Carrancas Klippe, interference zone of the Neoproterozoic southern Brasília and Ribeira orogens, SE Brazil. J. S. Am. Earth Sci. 103, 102744.
Cawood, P.A., Hawkesworth, C.J., Dhuime, B., 2013. The continental record and the generation of continental crust. Bulletin 125 (1–2), 14–32.
Cawood, P.A., Chowdhury, P., Mulder, J.A., Hawkesworth, C.J., Capitanio, F.A., Gunawardana, P.M., Nebel, O., 2022. Secular evolution of continents and the Earth system. Rev. Geophys. 60 (4), e2022RG000789.
Chakraborty, S., 2006. Diffusion modeling as a tool for constraining timescales of evolution of metamorphic rocks. Mineral. Petrol. 88 (1), 7–27.
Chamberlain, K.R., Bowring, S.A., 2001. Apatite–feldspar U–Pb thermochronometer: a reliable, mid-range (~ 450° C), diffusion-controlled system. Chem. Geol. 172 (1–2), 173–200.
Cherniak, D.J., 2000. Pb diffusion in rutile. Contrib. Miner. Petrol. 139, 198–207.
Chew, D.M., Spikings, R.A., 2015. Geochronology and thermochronology using apatite. Time and temperature, lower crust to surface. Elements 11, 189–194.
Chowdhury, P., Chakraborty, S., 2019. Slow cooling at higher temperatures recorded within high-P mafic granulites from the Southern Granulite Terrain, India: implications for the presence and style of plate tectonics near the Archean–Proterozoic boundary. J. Petrol. 60 (3), 441–486.
Chowdhury, P., Chakraborty, S., Gerya, T.V., Cawood, P.A., Capitanio, F.A., 2020. Peel-back controlled lithospheric convergence explains the secular transitions in Archean metamorphism and magmatism. Earth Planet. Sci. Lett. 538, 116224.
Chowdhury, P., Chakraborty, S., Gerya, T.V., 2021. Time will tell. Secular change in metamorphic timescales and the tectonic implications. Gondw. Res. 93, 291–310.
Cioffi, C.R., Campos Neto, M.C., Möller, A., Rocha, B.C., 2016a. Paleoproterozoic continental crust generation events at 2.08 and 2.15 Ga in the basement of the southern Brasília Orogen. SE Brazil. Precambrian Research 275, 176–196.
Cioffi, C.R., Campos Neto, M.C., Rocha, B.C., Moraes, R., Henrique-Pinto, R., 2012. Geochemical signatures of metasedimentary rocks of high-pressure granulite facies and their relation with partial melting. Carvalhos Klippe, Southern Brasília Belt, Brazil. J. S. Am. Earth Sci. 40, 63–76.
Cioffi, C.R., Neto, M.D.C.C., Möller, A., Rocha, B.C., 2016b. Tectonic significance of the Meso-to Neoarchean complexes in the basement of the southern Brasília Orogen. Precambrian Research 287, 91–107.
Cioffi, C.R., Neto, M.D.C.C., Möller, A., Rocha, B.C., 2019. Titanite petrochronology of the southern Brasília Orogen basement. Effects of retrograde net-transfer reactions on titanite trace element compositions. Lithos 344, 393–408.
Clark, C., Fitzsimons, I.C., Healy, D., Harley, S.L., 2011. How does the continental crust get really hot? Elements 7 (4), 235–240.
Coelho, M.B., Trouw, R.A.J., Ganade, C.E., Vinagre, R., Mendes, J.C., Sato, K., 2017. Constraining timing and P-T conditions of continental collision and late overprinting in the Southern Brasília Orogen (SE-Brazil). U-Pb zircon ages and geothermobarometry of the Andrelândia Nappe System. Precambr. Res. 292, 194–215.
Cordani, U.G., Brito-Neves, B.B., D'Agrella-Filho, M.S., 2003. From Rodinia to Gondwana: a review of the available evidence from South America. Gondw. Res. 6 (2), 275–283.
Cottle, J.M., Searle, M.P., Horstwood, M.S.A., Waters, D.J., 2009. Timing of mid-crustal metamorphism, melting and deformation in the Mt. Everest region of southern Tibet revealed by U-Th-Pb geochronology. J. Geol. 117, 643–664.
Ding, L., Zhong, D., Yin, A., Kapp, P., Harrison, T.M., 2001. Cenozoic structural and metamorphic evolution of the eastern Himalayan syntaxis (Namche Barwa). Earth Planet. Sci. Lett. 192 (3), 423–438.
Dumond, G., Goncalves, P., Williams, M.L., Jercinovic, M.J., 2015. Monazite as a monitor of melting, garnet growth and feldspar recrystallization in continental lower crust. J. Metam. Geol. 33, 735–762.
Engi, M., Lanari, P., Kohn, M.J., 2017. Significant ages—An introduction to petrochronology. Rev. Mineral. Geochem. 83 (1), 1–12.
Ewing, T.A., Hermann, J., Rubatto, D., 2013. The robust ness of the Zr-in-rutile and Ti-in-zircon thermometers during high-temperature metamorphism (Ivrea-Verbano Zone, north ern Italy). Contrib. Miner. Petrol. 165, 757–779.
Finger, F., Krenn, E., 2007. Three metamorphic monazite generations in a high-pressure rock from the Bohemian Massif and the potentially important role of apatite in stimulating polyphaser monazite growth along a PT loop. Lithos 95, 103–115.
Foster, G., Parrish, R.R., 2003. Metamorphic monazite and the generation of PTt paths. Geochem. Soc. Spec. Publ. 220, 25–47.
Foster, G., Kinny, P., Vance, D., Prince, C., Harris, N., 2000. The significance of monazite U–Th–Pb age data in metamorphic assemblages; a combined study of monazite and garnet chronometry. Earth Planet Science Letters 181, 327–340.
Fumes, R.A., Luvizotto, G.L., Moraes, R., Lanari, P., Valeriano, C.M., Zack, T., Caddick, M.J., Simões, L.S.A., 2022. Petrochronology of high-pressure granulite facies rocks from Southern Brasília Orogen, SE Brazil: Combining quantitative compositional mapping, single-element thermometry and geochronology. J. Metam. Geol. 40 (3), 517–552.
Frugis, G.L., Campos Neto, M.C., Lima, R.B., 2018. Eastern Paranapanema and southern São Francisco orogenic margins. Records of enduring Neoproterozoic oceanic convergence and collision in southern Brasília Orogen. Precambr. Res. 308, 35–57.
Fuck, R.A., Pimentel, M.M., Alvarenga, C.J.S., Dantas, E.L. 2017. The Northern Brasília Belt. In. Heilbron, M., Cordani, U.G., Alkmim, F.F. (Eds). São Francisco Craton, Eastern Brazil. Regional Geology Reviews, Springer, 205-220.
Garcia, M.D.G.M., Neto, M.D.C.C., 2003. Contrasting metamorphic conditions in the Neoproterozoic collision-related Nappes south of São Francisco Craton, SE Brazil. J. S. Am. Earth Sci. 15 (8), 853–870.
Gray, D. R., Foster, D. A., Meert, J. G., Goscombe, B. D., Armstrong, R., Trouw, R. A. J., & Passchier, C. W. 2008. A Damara orogen perspective on the assembly of southwestern Gondwana.
Hacker, B.R., Kylander-Clark, A.R.C., Holder, R.M., Andersen, T.B., Peterman, E.M., Walsh, E.O., Munnikhuis, J.K., 2015. Monazite response to ultrahigh-pressure subduction from U-Pb dating by laser ablation split stream. Chem. Geol. 409, 28–41.
Hacker, B., Kylander-Clark, A., Holder, R., 2019. REE partitioning between monazite and garnet. Implications for petrochronology. J. Metam. Geol. 37 (2), 227–237.
Harlov, D.E., Hetherington, C.J., 2010. Partial high-grade alteration of monazite using alkali-bearing fluids. Experiment and Nature. American Mineralogist 95 (7), 1105–1108.
Hermann, J., Rubatto, D., 2003. Relating zircon and monazite domains to garnet growth zones: age and duration of granulite facies metamorphism in the Val Malenco lower crust. J. Metam. Geol. 21, 833–852.
Hogmalm, K.J., Zack, T., Karlsson, A.K.O., Sjöqvist, A.S., Garbe-Schönberg, D., 2017. In situ Rb–Sr and K–Ca dating by LA-ICP-MS/MS: an evaluation of N 2 O and SF 6 as reaction gases. J. Anal. At. Spectrom 32 (2), 305–313.
Holder, R.M., Hacker, B.R., Kylander-Clark, A.R., Cottle, J.M., 2015. Monazite trace-element and isotopic signatures of (ultra) high-pressure metamorphism. examples from the Western Gneiss Region. Norway. Chemical Geology 409, 99–111.
Holder, R.M., Yakymchuk, C., Viete, D.R., 2020. Accessory mineral Eu anomalies in suprasolidus rocks. beyond feldspar. Geochem. Geophys. Geosyst. 21 (8), e2020GC009052.
Jäger, E., 1977. Introduction to geochronology. In: Jäger, E., Hunziker, J. (Eds.), Lectures of Isotope Geology. Springer, Heidelberg, pp. 1–12.
Johnson, T.E., Clark, C., Taylor, R.J., Santosh, M., Collins, A.S., 2015. Prograde and retrograde growth of monazite in migmatites. an example from the Nagercoil Block, southern India. Geosci. Front. 6 (3), 373–387.
Kelsey, D.E., Clark, C., Hand, M., 2008. Thermobarometric modelling of zircon and monazite growth in melt-bearing systems: examples using model metapelitic and metapsammitic granulites. J. Metam. Geol. 26 (2), 199–212.
Kohn, M.J., Corrie, S.L., Markley, C., 2015. The fall and rise of metamorphic zircon. Am. Mineral. 100 (4), 897–908.
Kohn, M.J., Penniston-Dorland, S.C., 2017. Diffusion: obstacles and opportunities in petrochronology. Rev. Mineral. Geochem. 83 (1), 103–152.
Kooijman, E., Mezger, K., Berndt, J., 2010. Constraints on the U-Pb systematics of me tamorphic rutile from in situ LA-ICP-MS analysis. Earth Planet. Sci. Lett. 293, 321–330.
Kuster, K., Ribeiro, A., Trouw, R.A., Dussin, I., Marimon, R.S., 2020. The Neoproterozoic Andrelândia group. Evolution from an intraplate continental margin to an early collisional basin south of the São francisco craton. Brazil. Journal of South American Earth Sciences 102, 102666.
Kylander-Clark, A.R., Hacker, B.R., Cottle, J.M., 2013. Laser-ablation split-stream ICP petrochronology. Chem. Geol. 345, 99–112.
Kylander-Clark, A.R., 2017. Petrochronology by laser-ablation inductively coupled plasma mass spectrometry. Rev. Mineral. Geochem. 83 (1), 183–198.
Li, B., Massonne, H.J., Hartmann, L.A., Zhang, J., Luo, T., 2021. Kyanite-garnet granulite from the Andrelândia nappe system, Brasília belt, registers two late Neoproterozoic metamorphic cycles. Precambr. Res. 355, 106086.
Li, S.S., Palin, R.M., Santosh, M., 2023. Contrasting mechanisms and timescales of subduction and exhumation as recorded by Paleoproterozoic and late Paleozoic high-pressure granulites in the North China Craton. GSA Bull. 135 (1–2), 29–47.
Liu, J.H., Lanari, P., Tamblyn, R., Dominguez, H., Hermann, J., Rubatto, D., Guo, J., 2025. Ultra-fast metamorphic reaction during regional metamorphism. Geochim. Cosmochim. Acta 394, 106–125.
Lotout, C., Poujol, M., Pitra, P., Anczkiewicz, R., Van Den Driessche, J., 2020. From burial to exhumation: emplacement and metamorphism of mafic eclogitic terranes constrained through multimethod petrochronology, case study from the Lévézou Massif (French Massif Central, Variscan Belt). J. Petrol. 61 (4), egaa046.
Lotout, C., Indares, A., Vervoort, J., Deloule, E., 2023. High-P metamorphism in the Mesoproterozoic. Petrochronological insights from the Grenville Province. Precambr. Res. 399, 107208.
Marimon, R.S., Trouw, R.A.J., Dantas, E.L., Ribeiro, A., Santos, P., Kuster, K., Vinagre, R., 2021. Provenance of passive-margin and syn-collisional units: implications for the geodynamic evolution of the southern Brasília orogen. West Gondwana. Sedimentary Geology 413, 105823.
Marimon, R.S., Hawkesworth, C.J., Trouw, R.A.J., Trouw, C., Dantas, L., Ribeiro, A., Vinagre, R., Hackspacher, P., Avila, C., Motta, R., Moraes, R., 2022. Subduction and continental collision in the Neoproterozoic. Sanukitoid-like magmatism and paired metamorphism in SE Brazil. Precambr. Res. 383, 106888 https://doi.org/10.1016/j.precamres.2022.106888.

Marimon, R.S., Trouw, R.A., Hawkesworth, C.J., Waterkemper, J., Ribeiro, A., Vinagre, R., Dantas, E.L., 2023. Challenges of dating metasedimentary successions in collisional orogens. a case study of a Neoproterozoic passive margin in West Gondwana. Gondw. Res. 113, 1–13.
McDonough, W.F., Sun, S.S., 1995. The composition of the Earth. Chem. Geol. 120 (3–4), 223–253.
Möller, A., Mezger, K., Schenk, V., 2000. U–Pb dating of metamorphic minerals. Pan-african metamorphism and prolonged slow cooling of high pressure granulites in Tanzania, East Africa. Precambr. Res. 104 (3–4), 123–146.
Mora, C.A.S., Campos Neto, M.C., Basei, M.A.S., 2014. Syn-collisional lower continental crust anataxis in the Neoproterozoic Socorro-Guaxupé Nappe System, southern Brasília Orogen, Brazil: constraints from zircon U-Pb dating, Sr-Nd-Hf signatures and whole-rock geochemistry. Precambr. Res. 255, 847–864.
Motta, R.G., Moraes, R., 2017. Pseudo- and real-inverted metamorphism caused by the superposition and extrusion of a stack of nappes: a case study of the Southern Brasília Orogen. Brazil. International Journal of Earth Sciences 106 (7), 2407–2427.
Motta, R.G., Fitzsimons, I.C., Moraes, R., Johnson, T.E., Schuindt, S., Benetti, B.Y., 2021. Recovering P–T–t paths from ultra-high temperature (UHT) felsic orthogneiss: an example from the Southern Brasília Orogen. Brazil. Precambrian Research 359, 106222.
Mottram, C.M., Parrish, R.R., Regis, D., Warren, C.J., Argles, T.W., Harris, N.B., Roberts, N.M., 2015. Using U-Th-Pb petrochronology to determine rates of ductile thrusting. Time windows into the Main Central Thrust, Sikkim Himalaya. Tectonics 34 (7), 1355–1374.
O'Brien, P.J., Rötzler, J., 2003. High-pressure granulites: formation, recovery of peak conditions and implications for tectonics. J. Metam. Geol. 21 (1), 3–20.
O'brien, P.J., 2008. Challenges in high-pressure granulite metamorphism in the era of pseudosections: reaction textures, compositional zoning and tectonic interpretation with examples from the Bohemian Massif. J. Metam. Geol. 26 (2), 235–251.
Oriolo, S., Wemmer, K., Oyhantçabal, P., Fossen, H., Schulz, B., Siegesmund, S., 2018. Geochronology of shear zones–a review. Earth Sci. Rev. 185, 665–683.
Pyle, J.M., Spear, F.S., 2003. Four generations of accessory-phase growth in low-pressure migmatites from SW New Hampshire. Am. Mineral. 88, 338–351.
Reno, B.L., Brown, M., Kobayashi, K., Nakamura, E., Piccoli, P.M., Trouw, R.A.J., 2009. Eclogite-high-pressure granulite metamorphism records early collision in West Gondwana: new data from the Southern Brasília Belt, Brazil. J. Geol. Soc. Lond. 166, 1013–1032.
Reno, B.L., Brown, M., Piccoli, P.M., 2010. 40Ar/39Ar thermochronology of high-pressure granulite nappes in the southern Brasília belt, Brazil. Implications for nappe exhumation. Am. J. Sci. 310 (10), 1294–1332.
Reno, B.L., Piccoli, P.M., Brown, M., Trouw, R.A.J., 2012. In situ monazite (U–Th)–Pb ages from the Southern Brasília Belt, Brazil: constraints on the high-temperature retrograde evolution of HP granulites. J. Metam. Geol. 30 (1), 81–112.
Ribeiro, B.V., Mulder, J.A., Faleiros, F.M., Kirkland, C.L., Cawood, P.A., O'Sullivan, G., Nebel, O., 2020. Using apatite to resolve the age and protoliths of mid-crustal shear zones. a case study from the Taxaquara Shear Zone, SE Brazil. Lithos 378, 105817.
Ribeiro, B.V., Finch, M.A., Cawood, P.A., Faleiros, F.M., Murphy, T.D., Simpson, A., Barrote, V.R., 2022. From microanalysis to supercontinents: insights from the Rio Apa Terrane into the Mesoproterozoic SW amazonian Craton evolution during Rodinia assembly. J. Metam. Geol. 40 (4), 631–663.
Ribeiro, B.V., Kirkland, C.L., Kelsey, D.E., Reddy, S.M., Hartnady, M.I.H., Faleiros, F.M., Rankenburg, K., Liebmann, J., Korhonen, F.J., Clark, C., 2023. Time-strain evolution of shear zones from petrographically constrained Rb-Sr muscovite analysis. Earth Planet. Sci. Lett. 602, 117969.
Ribeiro, B.V., Kirkland, C.L., Smit, M., Musiyachenko, K., Korhonen, F.J., Evans, N.J., Makin, S., 2024. Garnet Reference Materials for In Situ Lu-Hf Geochronology. Geostand. Geoanal. Res. 48 (4), 887–908.
Rocha, B.C.D., Moraes, R.D., Möller, A., Cioffi, C.R., Jercinovic, M.J., 2017. Timing of anatexis and melt crystallization in the Socorro–Guaxupé Nappe, SE Brazil: insights from trace element composition of zircon, monazite and garnet coupled to UPb geochronology. Lithos 277, 337–355.
Rocha, B.C., Moraes, R., Möller, A., Cioffi, C.R., 2018. Magmatic inheritance vs. UHT metamorphism. Zircon petrochronology of granulites and petrogenesis of charnockitic leucosomes of the Socorro-Guaxupé Nappe. SE Brazil. Lithos 314–315, 16–39.
Rocha, B.C., Neto, M.C.C., Cioffi, C.R., Westin, A., Alves, A., Salazar-Mora, C.A., Maurer, V.C., 2024a. The passive margin of the southern São Francisco paleocontinent, metamorphic record and implications for the assembly of West Gondwana. evidence from the Lima Duarte Nappe, Ribeira Orogen (SE Brazil). Precambr. Res. 404, 107338.
Rocha, B.C., Neto, M.C.C., Cioffi, C.R., Westin, A., Alves, A., Salazar-Mora, C.A., Maurer, V.C., 2024b. Reply to comment on "the passive margin of the southern São Francisco paleocontinent, metamorphic record and implications for the assembly of West Gondwana. evidence from the Lima Duarte Nappe, Ribeira orogen (SE Brazil)" by Trouw and Ribeiro. Precambr. Res. 411, 107523.
Rösel, D., Zack, T., 2022. LA-ICP-MS/MS Single-Spot Rb-Sr Dating. Geostand. Geoanal. Res. 46 (2), 143–168.
Rossi-Vieira, P.L.N.D.C., Tedeschi, M., Rocha, B.C.D., Lana, C.C., Barrote, V., Pedrosa-Soares, A.C., Alkmim, A., 2023. Detrital zircon U–Pb-Hf isotopes-based reconstruction of the depositional history of (ultra) high-temperature metamorphic rocks from the Socorro-Guaxupé Nappe (southern Brasília orogen, Brazil). J. S. Am. Earth Sci. 128, 104469.
Rubatto, D., Hermann, J., Buick, I.S., 2006. Temperature and bulk composition control on the growth of monazite and zircon during low-pressure anatexis (Mount Stafford, central Australia). J. Petrol. 47 (10), 1973–1996.
Rubatto, D., Chakraborty, S., Dasgupta, S., 2013. Timescales of crustal melting inthe Higher Himalayan Crystalines (Sikkim, Eastern Himalaya) inferred from trace element constrained monazite and zircon chronology. Contrib. Miner. Petrol. 165, 349–372.
Schoene, B., Bowring, S.A., 2007. Determining accurate temperature-time paths from U-Pb thermochronology. an example from the Kaapvaal craton, southern Africa. Geochim. Cosmochim. Acta 71, 165–185.
Schönig, J., 2024. Comment on:" Passive continental margin subducted to mantle depths. Coesite-bearing metasedimentary rocks from the neoproterozoic Brasília Orogen, west Gondwana margin". Precambr. Res. 412, 107558.
Seydoux-Guillaume, A.-M., Paquette, J.-L., Wiedenbeck, M., Montel, Heinrich, J-M., 2002. Experimental resetting of the U-Th-Pb systems in monazite. Chem. Geol. 191, 165–181.
Shrestha, S., Larson, K.P., Duesterhoeft, E., Soret, M., Cottle, J.M., 2019. Thermodynamic modelling of phosphate minerals and its implications for the development of PTt histories. a case study in garnet-monazite bearing metapelites. Lithos 334, 141–160.
Simpson, A., Gilbert, S., Tamblyn, R., Hand, M., Spandler, C., Gillespie, J., Nixon, A., Glorie, S., 2021. In-situ Lu-Hf geochronology of garnet, apatite and xenotime by LA-ICP-MS/MS. Chem. Geol. 577, 120299.
Smit, M.A., Scherer, E.E., Mezger, K., 2013. Lu–Hf and Sm–Nd garnet geochronology: chronometric closure and implications for dating petrological processes. Earth Planet. Sci. Lett. 381, 222–233.
Spear, F.S., Pyle, J.M., 2002. Apatite, monazite, and xenotime in metamorphic rocks. In. Kohn, M.J., Rakovan, J., Hughes, J.M. (Eds.), Phosphates. Geochemical, Geobiological, and Materials Importance, 48. Reviews in Mineralogy and Geochemistry, Mineralogical Society of America, Washington, D. C, 293–335.
Stacey, J.T., Kramers, 1975. Approximation of terrestrial lead isotope evolution by a two-stage model. Earth Planet. Sci. Lett. 26 (2), 207–221.
Strachan, R.A., Kirkland, C.L., Finlay, A.J., Wray, D.S., Metcalfe, J.H., Holdsworth, R.E., 2024. U–Pb apatite geochronology shows multiple thermal overprints within the Neoarchean foreland basement of the Faroe–Shetland Terrane. J. Geol. Soc. London 181 (5), jgs2024-003.
Tamblyn, R., Hand, M., Simpson, A., Gilbert, S., Wade, B., Glorie, S., 2022. In situ laser ablation Lu–Hf geochronology of garnet across the Western Gneiss Region: campaign-style dating of metamorphism. J. Geol. Soc. London 179 (4), jgs2021-094.
Tedeschi, M., Lanari, P., Rubatto, D., Pedrosa-Soares, A.C., Herman, J., Dussin, I., Pinheiro, M.A.P., Bouvier, S., Baumgartner, L., 2017. Reconstruction of multiple P-T-t stages from retrogressed mafic rocks: subduction versus collision in the Southern Brasília orogen (SE Brazil). Lithos 294–295, 283–303.
Tian, Z., Zhang, Z., Dong, X., 2019. Constraining the age of high-pressure metamorphism of paragneisses from the Eastern Himalayan Syntaxis using zircon petrochronology and phase equilibria. Geol. Soc. London Spec. Publ. 474, 331–352.
Tomkins, H.S., Powell, R., Ellis, D.J., 2007. The pressure dependence of the zirconium-in-rutile thermometer. J. Metam. Geol. 25 (6), 703–713.
Trouw, R.A.J., Ribeiro, A., Paciullo, F., 1983. Geologia estrutural dos Grupos São João Del Rei, Carrancas e Andrelândia, Sul de Minas Gerais. Anais Da Academia Brasileira De Ciências 55, 71–85.
Trouw, R.A.J., Heilbron, M., Ribeiro, A., Paciullo, F., Valeriano, C.M., Almeida, J.C.H., Tupinambá, M., Andreis, R.R., 2000. The central segment of Ribeira Belt. In. Cordani, U.G., Milani, E.J., Thomaz-Filho, A., Campos, D.A. (Eds.) Tectonic Evolution of South America. 287-310. 31th International Geological Congress. Rio de Janeiro, Brasil.
Trouw, R.A.J., Peternel, R., Ribeiro, A., Heilbron, M., Vinagre, R., Duffles, P., Trouw, C. C., Fontainha, M., Kussama, H.H., 2013. A new interpretation for the interference zone between Southern Brasília belt and the central Ribeira belt, SE Brazil. J. S. Am. Earth Sci. 48, 43–57.
Valeriano, C.M., Pimentel, Heilbron, M.M., Almeida, M., Trouw, J.C.H., 2008. Tectonic Evolution of the Brasília Belt, Central Brazil, and early assembly of Gondwana. Geol. Soc. Lond. Spec. Publ. 294, 197–210.
Valeriano, C.M., 2017. The Southern Brasília Belt. In. Heilbron, M., Cordani, U.G., Alkmim, F.F. (Eds). São Francisco Craton, Eastern Brazil. Regional Geology Reviews, Springer, 189-203.
Verschure, R.H., Andriessen, P.A.M., Boelrijk, N.A.I.M., Hebeda, E.H., Maijer, C., Priem, H.N.A., Verdurmen, E.T., 1980. On the thermal stability of Rb-Sr and K-Ar biotite systems: evidence from coexisting Sveconorwegian (ca 870 Ma) and Caledonian (ca 400 Ma) biotites in SW Norway. Contrib. Miner. Petrol. 74, 245–252.
Vielzeuf, D., Schmidt, M.W., 2001. Melting relations in hydrous systems revisited: application to metapelites, metagreywackes and metabasalts. Contrib. Miner. Petrol. 141 (3), 251.
Vinagre, R., Trouw, R.A.J., Mendes, J.C., Duffles, P., Peternel, R., Matos, G., 2014. New evidence of a magmatic arc in the Southern Brasília Belt, Brazil. the Serra da Água Limpa batholith (Socorro-Guaxupé Nappe). J. S. Am. Earth Sci. 54, 120–139.
Vry, J.K., Baker, J.A., 2006. LA-MC-ICPMS Pb-Pb dating of rutile from slowly cooled granulites. Confirmation of the high closure temperature for Pb diffusion in rutile. Geochim. Cosmochim. Acta 70, 1807–1820.
Wang, S., Brown, M., Wang, L., Johnson, T.E., Olierook, H.K., Kirkland, C.L., McDonald, B.J., 2023a. Two-stage exhumation of deeply subducted continental crust. Insight from zircon, titanite, and apatite petrochronology, Sulu belt of eastern China. Bulletin 135 (1–2), 48–66.
Wang, D., Guo, J., 2017. Late Archean high-pressure pelitic granulites in the Yinshan block, North China Craton. Precambr. Res. 303, 251–267.
Wang, D., Mitchell, R.N., Guo, J., Liu, F., 2023b. Exhumation of an Archean granulite terrane by paleoproterozoic orogenesis: evidence from the North China Craton. J. Petrol. 64 (6), egad035.

Wang, J.M., Rubatto, D., Zhang, J.J., 2015. Timing of Partial Melting and Cooling across the Greater Himalayan Crystalline complex (Nyalam, Central Himalaya): In-sequence Thrusting and its Implications. J. Petrol. 56, 1677–1702.
Wang, J.M., Wu, F.Y., Rubatto, D., Liu, S.R., Zhang, J.J., Liu, X.C., Yang, L., 2017. Monazite behaviour during isothermal decompression in pelitic granulites: a case study from Dinggye, Tibetan Himalaya. Contrib. Miner. Petrol. 172, 81.
Wang, J.M., Rubatto, D., Lanari, P., Tian, Y.L., Chen, Y., Wu, F.Y., 2024. Low total REE zircon formed in equilibrium with hornblende in granulitized eclogites: Implications for exhumation rates. Earth Planet. Sci. Lett. 648, 119084.
Wawrzenitz, N., Krohe, A., Baziotis, I., Mposkos, E., Kylander-Clark, A.R., Romer, R.L., 2015. LASS U–Th–Pb monazite and rutile geochronology of felsic high-pressure granulites (Rhodope, N Greece). Effects of fluid, deformation and metamorphic reactions in local subsystems. Lithos 232, 266–285.
Westin, A., Neto, M.C.C., Hawkesworth, C.J., Cawood, P.A., Dhuime, B., Delavault, H., 2016a. A paleoproterozoic intra-arc basin associated with a juvenile source in the Southern Brasilia Orogen. Application of U–Pb and Hf–Nd isotopic analyses to provenance studies of complex areas. Precambr. Res. 276, 178–193.
Westin, A., Campos Neto, M.C., Cawood, P., Hawkesworth, C., Dhuime, B., Delavault, H., 2019. The Neoproterozoic southern passive margin of the São Francisco craton: insights on the pre-amalgamation of West Gondwana from U-Pb and Hf-Nd isotopes. Precambr. Res. 320, 454–471.
Westin, A., Campos Neto, M.C., Hawkesworth, C., Cawood, P., Dhuime, B., Delavault, H., 2016b. A Paleoproterozoic intra-arc basin associated with a juvenile source in the southern Brasília Orogen: using U-Pb ages and Hf-Nd isotopic analyses in provenance studies of complexes areas. Precambr. Res. 276, 178–193.
Whitney, D.L., Evans, B.W., 2010. Abbreviations for names of rock-forming minerals. Am. Mineral. 95 (1), 185–187.
Williams, M.L., Jercinovic, M.J., Hetherington, C.J., 2007. Microprobe monazite geochronology: understanding geologic processes by integrating composition and chronology. Annu. Rev. Earth Planet. Sci. 35 (1), 137–175.
Xu, Y., Holder, R.M., Viete, D.R., 2025. Contrasting cooling histories in the Archean Minnesota River Valley Subprovince of the Superior Craton of North America with implications for secular change of metamorphic time scales. Geol. Soc. Am. Bull.
Yakymchuk, C., Brown, M., 2014. Behaviour of zircon and monazite during crustal melting. J. Geol. Soc. London 171 (4), 465–479.
Yakymchuk, C., Brown, M., 2019. Divergent behaviour of Th and U during anatexis. Implications for the thermal evolution of orogenic crust. J. Metam. Geol. 37 (7), 899–916.
Yakymchuk, C., 2017. Behaviour of apatite during partial melting of metapelites and consequences for prograde suprasolidus monazite growth. Lithos 274, 412–426.
Zack, T., Hogmalm, K.J., 2016. Laser ablation Rb/Sr dating by online chemical separation of Rb and Sr in an oxygen-filled reaction cell. Chem. Geol. 437, 120–133.